Relic Gravitational Waves from the Chiral Magnetic Effect

Axel Brandenburg[1,2,3,4] , Yutong He[1,2] , Tina Kahniashvili[3,4,5] , Matthias Rheinhardt[6] , and Jennifer Schober[7]

[1] Nordita, KTH Royal Institute of Technology and Stockholm University, Hannes Alfvéns väg 12, SE-10691 Stockholm, Sweden
[2] Department of Astronomy, AlbaNova University Center, Stockholm University, SE-10691 Stockholm, Sweden
[3] McWilliams Center for Cosmology and Department of Physics, Carnegie Mellon University, 5000 Forbes Avenue, Pittsburgh, PA 15213, USA
[4] Faculty of Natural Sciences and Medicine, Ilia State University, 3-5 Cholokashvili Avenue, 0194 Tbilisi, Georgia
[5] Department of Theoretical Astrophysics and Cosmology, Abastumani Astrophysical Observatory, 47/57 Kostava Street, 0179 Tbilisi, Georgia
[6] Department of Computer Science, Aalto University, PO Box 15400, FI-00076 Aalto, Finland
[7] Laboratoire d'Astrophysique, EPFL, CH-1290 Sauverny, Switzerland

Abstract

Relic gravitational waves (GWs) can be produced by primordial magnetic fields. However, not much is known about the resulting GW amplitudes and their dependence on the details of the generation mechanism. Here we treat magnetic field generation through the chiral magnetic effect (CME) as a generic mechanism and explore its dependence on the speed of generation (the product of magnetic diffusivity and characteristic wavenumber) and the speed characterizing the maximum magnetic field strength expected from the CME. When the latter exceeds the former (regime I), which is the regime applicable to the early universe, we obtain an inverse cascade with moderate GW energy that scales with the third power of the magnetic energy. When the generation speed exceeds the CME limit (regime II), the GW energy continues to increase without a corresponding increase of magnetic energy. In the early kinematic phase, the GW energy spectrum (per linear wavenumber interval) has opposite slopes in both regimes and is characterized by an inertial range spectrum in regime I and a white noise spectrum in regime II. The occurrence of these two slopes is shown to be a generic consequence of a nearly monochromatic exponential growth of the magnetic field. The resulting GW energy is found to be proportional to the fifth power of the limiting CME speed and the first power of the generation speed.

1. Introduction

The chiral magnetic effect (CME) describes an electric current along a magnetic field carried by electrically charged chiral fermions (Vilenkin 1980). This effect has been discussed as one of several possible mechanisms for significantly amplifying primordial magnetic fields in the early universe (Boyarsky et al. 2012, 2015). It works as a dynamo effect that destabilizes the state of a vanishing magnetic field and causes an arbitrarily weak seed field to grow exponentially for a limited time (Joyce & Shaposhnikov 1997). Excitation sets in when the fermion chiral asymmetry is large enough. However, owing to the existence of a conservation law for the sum of magnetic helicity and chiral asymmetry, the CME becomes continuously depleted until nearly all the initial chiral asymmetry turns into magnetic helicity (Boyarsky et al. 2012, 2015). Thus, the initial chiral asymmetry determines the final value of the product of the mean-squared magnetic field $B_{\rm rms}^2$ and the magnetic correlation length $\xi_{\rm M}$, forming a proxy for magnetic helicity in case of a fully helical field. For realistic parameters describing our universe, $B_{\rm rms}^2 \xi_{\rm M}$ is expected to be of the order of or below $(10^{-18}\,{\rm G})^2$ Mpc (Brandenburg et al. 2017b). This value is below the lower limit of $B_{\rm rms}^2 \xi_{\rm M} > (10^{-16}\,{\rm G})^2$ Mpc, which is inferred from the non-observations of GeV-energy halos around TeV blazars (Aharonian et al. 2006; Neronov & Vovk 2010; Taylor et al. 2011). Yet the question can be raised, whether the resulting magnetic stress could still be large enough to produce measurable gravitational waves (GWs).

Another severe problem are the very small length scales associated with the CME. An upper bound for the wavenumber associated with the chiral asymmetry in comoving units is

$k_* \equiv k_{\rm B} T / \hbar c = 12\,{\rm cm}^{-1}$, where $k_{\rm B}$ is the Boltzmann constant, $\hbar$ is the reduced Planck constant, c is the speed of light, and $T = 2.7$ K is the present-day temperature. Assuming a field strength of $1\,\mu$G, the value of k_* is compatible with the upper bound on the magnetic helicity of $(10^{-18}\,{\rm G})^2$ Mpc (Brandenburg et al. 2017b). This value of k_* corresponds to very small length scales because the CME is a microphysical effect involving just $\hbar$, c, and $k_{\rm B}$ as relevant natural constants, but not Newton's constant or the Planck mass; see also Brandenburg et al. (2017a). The Hubble radius, by contrast, does involve Newton's constant and is much bigger (1.8×10^{15} cm). In units of the inverse Hubble radius, the characteristic scale of the CME corresponds to a wavenumber of about 2×10^{16} (see Equation (1) of Kahniashvili et al. 2013) and is associated with a very high GW frequency of 4×10^{11} Hz; see Equation (51) of Kosowsky et al. (2002). On the other hand, at the time of the electroweak phase transition, the Hubble scale corresponds to a frequency in the millihertz range, which is the range accessible to the Laser Interferometer Space Antenna. Larger length scales have been argued to be possible by invoking a strongly out-of-equilibrium magnetic field generation during preheating (Díaz-Gil et al. 2008a, 2008b) or during inflation (Sharma et al. 2020; Okano & Fujita 2021). In addition, the actual GW frequency could be several orders of magnitude smaller owing to the inverse cascade associated with the CME. By the time the magnetic field has reached its maximum, its typical length scale can therefore be significantly larger than the scale at which the field was originally produced. After that time, the magnetic length scales continue to increase as the magnetic energy decreases. However, Roper Pol et al. (2020b) found that the resulting GW energy is determined by just the maximum field strength.

It is therefore unclear whether the late phase of magnetic decay is still relevant to GW production.

Although the CME may not open a viable pathway for explaining the primordial magnetic field, it has the advantage of providing a self-consistent mechanism for explaining not just a certain field strength and length scale, but also a certain time dependence of its generation, independent of any additional assumptions. Thus, it may serve as a proxy for other generation mechanisms. It is then interesting to investigate GWs produced by the CME as a mechanism that is likely to contain qualitatively valid aspects of primordial magnetic field generation; see the recent work by Anand et al. (2019) for analytic approaches addressing GW production from the CME at energies much above the electroweak scale, or the approaches of Sharma et al. (2020) and Okano & Fujita (2021) addressing GW production from helical magnetogenesis during inflation. These works provide more optimistic prospects for the resulting magnetic field generation than Brandenburg et al. (2017b) did. Therefore, in the present study our aim is to understand the detailed relationship between the strengths of the magnetic field and GWs, as well as their typical time and length scales.

In the past, theoretical GW energy spectra have been calculated mostly using analytical approaches; see Deryagin et al. (1987) for an early pioneering investigation and Caprini et al. (2019) for a recent review. Numerical approaches have recently been applied to GWs, driven by acoustic turbulence from first order phase transitions (Hindmarsh et al. 2015). A general uncertainty in simulating relic GWs from primordial turbulent sources is due to our ignorance about suitable initial conditions or generation mechanisms. When a turbulent state is invoked as an initial condition, the GW amplitude is determined almost entirely by the fact that then the GW source, i.e., the turbulent stress, jumps instantaneously from zero to a finite value (Roper Pol et al. 2020a). By contrast, when driving turbulence gradually by applying some forcing in the magnetohydro-dynamic (MHD) equations, the resulting GW amplitude depends on the details of how the turbulence develops and later declines; see Kahniashvili et al. (2021) for a more systematic invest-igation. These problems motivate our present study of GWs from the CME, too.

A number of interesting aspects of turbulence from the CME are already known. In particular, depending on the relative rates of magnetic field generation, on the one hand, and depletion of the CME, on the other, different regimes of turbulence can be distinguished (Brandenburg et al. 2017b). If the depletion is low, the maximum magnetic field strength is high and a turbulent spectrum with an inertial range emerges before the turbulence starts to decay in a self-similar fashion. If the depletion is high, on the other hand, no turbulent inertial range develops. How the resulting GW amplitude depends on the governing parameters of the CME-driven field generation is unclear and illuminating this is the main purpose of this paper. Although the process is physically motivated, we choose parameters that are motivated by our attempt to understand the relationship between magnetic field generation and the resulting GWs in any conceivable regime. Our parameters are therefore not those relevant to the early universe, nor are they necessarily physically realizable. Nevertheless, the present work may prove to be important for guiding our intuition about GW production from primordial turbulent sources.

2. The Model

2.1. Basic Equations

The MHD equations for an ultrarelativistic quark-gluon plasma in a flat expanding universe in the radiation-dominated era after the electroweak phase transition can be written in terms of conformal time and comoving coordinates such that the expansion no longer appears explicitly (Brandenburg et al. 1996, 2017a; Durrer & Neronov 2013), except for the GW equation; see below. The bulk motions are assumed to be subrelativistic.

We quantify the chiral asymmetry through the imbalance between the number densities $n_{\rm L}$ and $n_{\rm R}$ of left- and right-handed fermions, respectively, as

$$\mu_5 = 24\,\alpha_{\rm em}\,(n_{\rm L} - n_{\rm R})\,(\hbar c/k_{\rm B}T)^2, \qquad (1)$$

employing the normalization used by Rogachevskii et al. (2017). Here, $\alpha_{\rm em}$ is the fine structure constant. The index 5 is commonly chosen in this context and reminiscent of the fifth Dirac matrix γ_5, central in defining particle chirality. We should point out that our μ_5 has a unit of inverse length and is related to the chiral chemical potential (with units of energy) through an extra $\hbar c/4\alpha_{\rm em}$ factor; see Schober et al. (2020).

We follow here the normalization of Roper Pol et al. (2020a, 2020b), where the Heaviside–Lorentz system of units is used for the magnetic field and the scale factor $a(t)$ is set to unity at the time t_* of the electroweak phase transition (denoted by an asterisk). The Hubble parameter H at t_* is $H_* = t_*^{-1}$. All quantities are made nondimensional by normalizing the time by t_*, velocities by the speed of light c, and the density ρ by the critical density $\rho_{\rm crit}$ for a flat universe. Spatial coordinates are then normalized by the Hubble scale c/H_*. Consequently, μ_5 is normalized by H_*/c. To obtain the comoving magnetic field in gauss, one has to multiply it by $\sqrt{4\pi\rho_{\rm crit}}\,c$.

The governing equations for the magnetic field $\boldsymbol{B}$ and μ_5 can then be written as (Rogachevskii et al. 2017; Schober et al. 2018)

$$\frac{\partial \boldsymbol{B}}{\partial t} = \boldsymbol{\nabla} \times [\boldsymbol{u} \times \boldsymbol{B} + \eta(\mu_5 \boldsymbol{B} - \boldsymbol{J})], \quad \boldsymbol{J} = \boldsymbol{\nabla} \times \boldsymbol{B}, \quad (2)$$

$$\frac{D\mu_5}{Dt} = -\lambda\,\eta(\mu_5 \boldsymbol{B} - \boldsymbol{J}) \cdot \boldsymbol{B} + D_5 \nabla^2 \mu_5 - \Gamma_{\rm f}\mu_5, \qquad (3)$$

where $D/Dt \equiv \partial/\partial t + \boldsymbol{u} \cdot \boldsymbol{\nabla}$ is the advective derivative, η is the magnetic diffusivity, λ characterizes the depletion of μ_5 as the magnetic field increases, D_5 is a chiral diffusion coefficient, and $\Gamma_{\rm f}$ is the flipping rate; see Boyarsky et al. (2021), for a recent calculation. These equations have been derived under the assumption $\eta \to 0$; see Rogachevskii et al. (2017) for details. Brandenburg et al. (2017b) found that for $k_{\rm B}T = 100\,{\rm GeV}$ and if μ_{50} is produced thermally, relevant to the time of the electroweak phase transition, $\Gamma_{\rm f}/\eta\mu_5^2 \approx 10^{-7}$, that is, the time $1/\Gamma_{\rm f}$ is much longer than the e-folding time of the fastest growing magnetic mode; see Section 2.2. Hence, we put $\Gamma_{\rm f} = 0$ from now on. The plasma velocity $\boldsymbol{u}$ and the density ρ (which includes the rest mass density) obey the momentum and energy

equations

$$\frac{D\boldsymbol{u}}{Dt} = \frac{2}{\rho}\boldsymbol{\nabla}\cdot(\rho\nu\mathbf{S}) - \frac{1}{4}\boldsymbol{\nabla}\ln\rho + \frac{\boldsymbol{u}}{3}(\boldsymbol{\nabla}\cdot\boldsymbol{u} + \boldsymbol{u}\cdot\boldsymbol{\nabla}\ln\rho)$$

$$- \frac{\boldsymbol{u}}{\rho}[\boldsymbol{u}\cdot(\boldsymbol{J}\times\boldsymbol{B}) + \eta\boldsymbol{J}^2] + \frac{3}{4\rho}\boldsymbol{J}\times\boldsymbol{B},$$

$$\frac{\partial\ln\rho}{\partial t} = -\frac{4}{3}(\boldsymbol{\nabla}\cdot\boldsymbol{u} + \boldsymbol{u}\cdot\boldsymbol{\nabla}\ln\rho) + \frac{1}{\rho}[\boldsymbol{u}\cdot(\boldsymbol{J}\times\boldsymbol{B}) + \eta\boldsymbol{J}^2],$$

(4)

where $\mathsf{S}_{ij} = (u_{i,j} + u_{j,i})/2 - \delta_{ij}\boldsymbol{\nabla}\cdot\boldsymbol{u}/3$ are the components of the rate-of-strain tensor with commas denoting partial derivatives, ν is the kinematic viscosity, and the ultrarelativistic equation of state $p = \rho/3$ has been employed. In the following, we assume uniform ν, η, and D_5 and vary them such that $\nu = \eta = D_5$.

The GW equation in the radiation era for the scaled strain tensor $\mathbf{h}$ with $\mathsf{h}_{ij} = a\mathsf{h}_{ij}^{\text{phys}}$ is written in Fourier space as (Roper Pol et al. 2020a, 2020b)

$$\frac{\partial^2}{\partial t^2}\tilde{h}_{+/\times}(\boldsymbol{k}, t) + k^2\tilde{h}_{+/\times}(\boldsymbol{k}, t) = \frac{6}{t}\tilde{T}_{+/\times}(\boldsymbol{k}, t),$$

(5)

where $\tilde{h}_{+/\times} = \mathsf{e}_{ij}^{+/\times}(\mathsf{P}_{il}\mathsf{P}_{jm} - \tfrac{1}{2}\mathsf{P}_{ij}\mathsf{P}_{lm})\,\tilde{h}_{lm}(\boldsymbol{k}, t)$ are the Fourier-transformed $+$ and $\times$ modes of $\mathbf{h}$, with $\mathsf{e}_{ij}^+(\boldsymbol{k}) = e_i^1 e_j^1 - e_i^2 e_j^2$ and $\mathsf{e}_{ij}^\times(\boldsymbol{k}) = e_i^1 e_j^2 + e_i^2 e_j^1$ being the linear polarization basis, $\boldsymbol{e}^1$ and $\boldsymbol{e}^2$ are unit vectors perpendicular to $\boldsymbol{k}$ and perpendicular to each other, and $\mathsf{P}_{ij}(\boldsymbol{k}) = \delta_{ij} - k_i k_j$ is the projection operator. $\tilde{T}_{+/\times}$ are defined analogously and normalized by the critical density. The stress is composed of magnetic and kinetic contributions, $\mathsf{T}_{ij} = \frac{4}{3}\gamma_{\text{Lor}}^2\rho u_i u_j - B_i B_j + ...$, where $\gamma_{\text{Lor}} = (1 - \boldsymbol{u}^2)^{-1/2}$ is the Lorentz factor, and the ellipsis denotes terms proportional to δ_{ij}, not contributing to $\tilde{T}_{+/\times}$. Since we use the nonrelativistic equations, we put $\gamma_{\text{Lor}} = 1$, except for one case shown in the Appendix, where $\gamma_{\text{Lor}} \neq 1$. Our equations apply to the time after the electroweak phase transition t_*, so our normalized time obeys $t \geqslant 1$. Furthermore, to compute the relic observable GW energy at the present time, we have to multiply $\mathcal{E}_{\text{GW}}^{\text{sat}}$ by the square of the ratio of the Hubble parameters and the fourth power of the ratio of scale factors between the moment of the electroweak phase transition and today, which is 1.64×10^{-5}; see Roper Pol et al. (2020a, 2020b) for details.

As already alluded to above, the system of Equations (2), (3) describing the CME must be regarded as partly phenomenological and subject to extensions and modifications. A purely helical magnetic field with wavenumber $k = \mu_5 = \text{const}$, for example, can never decay if $\Gamma_f = 0$, and yet it would lead to ohmic heating. However, those effects are not critical to the dynamics that we are concerned with in this paper and will therefore be ignored. Likewise, an extra $-\mu_5\boldsymbol{\nabla}\cdot\boldsymbol{u}$ term on the right-hand side of Equation (3) is necessary for a proper conservation equation. However, this would not make a noticeable difference because $\boldsymbol{\nabla}\cdot\boldsymbol{u}$ is always small; see the Appendix for a demonstration. It should also be noted that, in comparison with earlier work, this is the first time that the CME has been solved together with Equations (4), which contain additional $4/3$ factors. We refer to Appendix A of Brandenburg et al. (2017a) for the differences to standard MHD.

2.2. Basic Phenomenology of the Chiral Magnetic Effect

The CME introduces two important characteristic quantities into the system: λ and the initial value of μ_5, $\mu_{50} = \mu_5(t = 1)$, both assumed uniform. Different evolutionary scenarios can be envisaged depending on their values. Following Brandenburg et al. (2017b), we use the fact that λ^{-1} has the dimension of energy per unit length and μ_{50} has the dimension of inverse length, and identify two characteristic velocities:

$$v_\lambda = \mu_{50}/\lambda^{1/2}, \qquad v_\mu = \mu_{50}\eta. \tag{6}$$

We recall that here we have used dimensionless quantities. We can identify two regimes of interest:

$$\eta k_1 < v_\mu < v_\lambda \quad \text{(regime I)}, \tag{7}$$

$$\eta k_1 < v_\lambda < v_\mu \quad \text{(regime II)}, \tag{8}$$

where k_1 is the smallest wavenumber in the domain and $\eta k_1 < v_\mu$ is necessary for magnetic field excitation. The case of $v_\lambda < \eta k_1$ is highly diffusive and was not considered. In regime I, if the ratio $v_\lambda/v_\mu = [\eta\,\lambda^{1/2}]^{-1}$ is large, the λ term is unimportant, and μ_5 will only change slowly as the magnetic field grows. Once the magnetic field exceeds a critical value of around v_μ, it becomes turbulent; see Brandenburg et al. (2017b). In that paper, both v_μ and v_λ were assumed to be less than the speed of sound, but this is not a physically imposed constraint and will be relaxed in the present work. Brandenburg et al. (2017b) also found that the crossover between the regimes occurs when $v_\lambda/v_\mu \approx 8$. Regarding the resulting GW production, however, we shall find evidence for a crossover at $v_\lambda/v_\mu \approx 1$. One should also remember that v_μ and v_λ do not correspond to physically realizable speeds and are therefore not constrained to be below unity. Let us mention at this point that, using the calculation of Arnold et al. (2000) for the value of η and the expression $\lambda = 3\hbar c\,(8\alpha_{\text{em}}/k_{\text{B}}T)^2$ from Rogachevskii et al. (2017), Brandenburg et al. (2017b) estimated that $v_\mu \approx 2 \times 10^{-5}$ and $v_\lambda \approx 0.05$ for $\mu_{50} = 2 \times 10^{16}$.

If $\mu_{50} \neq 0$, the CME determines primarily the magnetic helicity that can subsequently be generated. This is a direct consequence of the conservation law for the (weighted) sum of mean magnetic helicity density and mean μ_5, i.e., the *total chirality* (Rogachevskii et al. 2017),

$$\tfrac{1}{2}\lambda\,\langle\boldsymbol{A}\cdot\boldsymbol{B}\rangle + \langle\mu_5\rangle = \text{const}, \tag{9}$$

where $\boldsymbol{A}$ with $\boldsymbol{B} = \boldsymbol{\nabla}\times\boldsymbol{A}$ is the magnetic vector potential, and the brackets denote averaging over a closed or periodic volume; see the Appendix for a discussion of the accuracy of Equation (9). If the initial magnetic helicity is arbitrarily small, the constant in Equation (9) can be set to μ_{50}. Neglecting the influence of the turbulent flow $\boldsymbol{u}$ and inhomogeneities of μ_5, the generated magnetic field is fully helical (Beltrami), and its helicity can be characterized by its wavenumber k_{M} and the mean magnetic energy density $\langle\boldsymbol{B}^2\rangle/2$ through $\langle\boldsymbol{A}\cdot\boldsymbol{B}\rangle \approx \langle\boldsymbol{B}^2\rangle/k_{\text{M}}$. Therefore, once all the initial μ_5 is used up, we have

$$\langle\boldsymbol{B}^2\rangle/k_{\text{M}} \approx 2\mu_{50}/\lambda. \tag{10}$$

Interestingly, the value of η does not enter this estimate. It does, however, determine the initial growth rate $\gamma(k)$ of the magnetic

field, which adopts its maximum, $\gamma_0 \equiv \eta\mu_{50}^2/4$, at the wavenumber $k_\mu \equiv \mu_{50}/2$. Using $k_M \approx k_\mu$, we expect

$$\langle \boldsymbol{B}^2 \rangle \lesssim \mu_{50}^2/\lambda \equiv v_\lambda^2, \tag{11}$$

so large magnetic fields are expected for large values of μ_{50} and small values of λ. The fact that v_λ characterizes the maximum magnetic field strength justifies the term "limiting CME speed." On the other hand, as one can express v_μ by the maximum growth rate and the corresponding wavenumber as $2\gamma_0/k_\mu$, we may call it "generation speed" in analogy to "phase speed" for a wave.

2.3. Magnetic Energy Spectrum from the CME

To estimate the amount of magnetic energy production from the CME, we adopt the semiempirical model of Brandenburg et al. (2017b), who proposed constructing the magnetic energy spectrum such that it had the k^{-2} slope that is characteristic of magnetically dominated turbulence, with energy injection predominantly at the wavenumber k_μ. For an intermediate time interval around the magnetic energy maximum, they then proposed the following form for the magnetic energy spectrum $E_M(k)$ (with normalization $\int E_M(k)dk = \langle \boldsymbol{B}^2 \rangle/2 \equiv \mathcal{E}_M$) as a function of wavenumber k and the parameters η, μ_{50}, and λ that govern the CME:

$$E_M(k) = C_5\,\mu_{50}^3\eta^2 k^{-2} \quad (k_\lambda \leqslant k \leqslant k_\mu), \tag{12}$$

where $C_5 \approx 16$ is a Kolmogorov-type constant,

$$k_\lambda = \sqrt{\lambda C_5/C_\lambda}\,\mu_{50}\eta \approx 4\mu_{50}\eta\lambda^{1/2} \tag{13}$$

is the wavenumber corresponding to the outer scale of the k^{-2} subrange, and $C_\lambda \approx 1$ is another empirical constant (Brandenburg et al. 2017b). Of course, Equation (12) can only hold if $k_\lambda \leqslant k_\mu$. In regime I, k_λ is the typical wavenumber of the magnetic field when it has reached maximum strength.

A detailed sketch illustrating the different spectral subranges is Figure 1 of Brandenburg et al. (2017b), who also confirmed the form of Equation (12) through simulations. The present simulations also support the existence of the different subranges.

2.4. GW Energy Scaling

The work of Roper Pol et al. (2020b) has shown that the GW energy is not just proportional to the square of the magnetic energy, but also proportional to the square of the dominating length scale (or inverse wavenumber) of $\boldsymbol{B}$. For example, their runs ini2 and ini3 have the same magnetic energy, but in ini3, the spectral peak was at a 10 times smaller wavenumber, corresponding to just 10 turbulent eddies per Hubble horizon. The resulting GW energy was then about 100 times larger. To leading order, the GW energy, normalized by the critical energy of the universe, is given by $\mathcal{E}_{GW} = \langle \dot{h}_+^2 + \dot{h}_\times^2 \rangle/6$; see Roper Pol et al. (2020a) for details regarding the $1/6$ factor and additional correction terms. Roper Pol et al. (2020b) studied different types of turbulence and confirmed the quadratic relationship between the maximum magnetic energy, $\mathcal{E}_M^{max}$, and the saturation value of the GW energy, $\mathcal{E}_{GW}^{sat}$, in the form

$$\mathcal{E}_{GW}^{sat} \approx (q\mathcal{E}_M^{max}/k_{peak})^2, \tag{14}$$

where k_{peak} is the wavenumber of the peak of the spectrum ($k_{peak} = 600$ in most of their cases, and 60 in the case where a

100 times larger $\mathcal{E}_{GW}^{sat}$ was found, suggesting an inverse quadratic relationship), and q is an empirical efficiency parameter that is about 0.9 for their cases with a turbulent initial MHD state (but no forcing), 1.8 in their simulations with forced MHD turbulence, and 11 in their simulations of forced acoustic turbulence, where $\mathcal{E}_M^{max}$ has to be replaced by the maximum *kinetic* energy. Larger values of q correspond to more efficient conversion of magnetic or kinetic energy into GW energy. The reason why acoustic turbulence is more efficient is unclear, but may be speculated to lie in its more vigorous time dependence.

2.5. Numerical Aspects

We solve Equations (2)–(5) using the PENCIL CODE (Pencil Code Collaboration et al. 2021), which is a finite difference code that is third order in time and sixth order in space, except that Equation (5) is solved exactly between subsequent time instants; see Roper Pol et al. (2020a) for details. For most of our simulations, we use 512^3 mesh points, which turned out to be sufficient for the present investigations. The lowest wavenumber in our computational domain, k_1, is chosen to be 100 for many of our runs. The side length of the cubical computational domain is then $2\pi/k_1$, which is chosen to be large enough so that the governing dynamics is well captured by the simulations, but small enough to resolve the smallest length scales. In many cases, we verified that the results are independent of the choice of k_1.

Throughout his work, we present spectra of various quantities. We denote this operation as Sp($\cdot$), which is performed as integration over concentric shells in wavenumber space. For a scalar quantity f, it reads as $\mathrm{Sp}(f(\boldsymbol{x})) = k^2 \int |\tilde{f}(\boldsymbol{k})|^2 d\Omega_k$, where Ω_k is the solid angle in $\boldsymbol{k}$ space, while for the tensor $\mathbf{h}$ we put $\mathrm{Sp}(\mathbf{h}) = \mathrm{Sp}(h_+) + \mathrm{Sp}(h_\times)$, and likewise for $\dot{\mathbf{h}}$ and $\mathbf{T}$. Thus, the GW energy spectrum is given by $E_{GW}(k) \equiv \mathrm{Sp}(\dot{\mathbf{h}})/6$ and the magnetic one by $E_M(k) \equiv [\mathrm{Sp}(B_x) + \mathrm{Sp}(B_y) + \mathrm{Sp}(B_z)]/2.$[8]

3. Results

We have performed a range of simulations where we vary η, λ, and μ_{50}, studying the influence of these parameters in turn.

3.1. Comparison with Earlier GW Energy Scaling

To put our new simulations into context, it is convenient to compare our values of $\mathcal{E}_{GW}^{sat}$ for a given $\mathcal{E}_M^{max}$ with those obtained by Roper Pol et al. (2020b). We show in Figure 1 a plot similar to their Figure 7, depicting our simulations with $\mu_{50} = 10^4$, grouped into four series with $\lambda^{1/2}$ in the range of 5×10^4 to 5×10^3. In each of those series, we vary η. The resulting values of $\mathcal{E}_M^{max}$ and $\mathcal{E}_{GW}^{sat}$ are summarized in Table 1, along with the four input parameters η, $\lambda^{1/2}$, μ_{50}, and k_1, as well as several derived quantities: ηk_1, v_μ, v_λ, $\eta\mu_{50}^2$, and k_λ (provided $k_\lambda \leqslant \mu_{50}/2$). In the last column, we also give according to Equation (14)

$$q = k_{peak}\sqrt{\mathcal{E}_{GW}^{sat}}\,/\mathcal{E}_M^{max}, \tag{15}$$

---

[8] Let us note in this connection that one commonly denotes the GW energy spectrum per *logarithmic* wavenumber interval by $\mathcal{E}_{GW}(k)$, which is distinguished from $\mathcal{E}_{GW}$ by the argument k. It is related to $E_{GW}(k)$ through $\mathcal{E}_{GW}(k) = kE_{GW}(k)$.

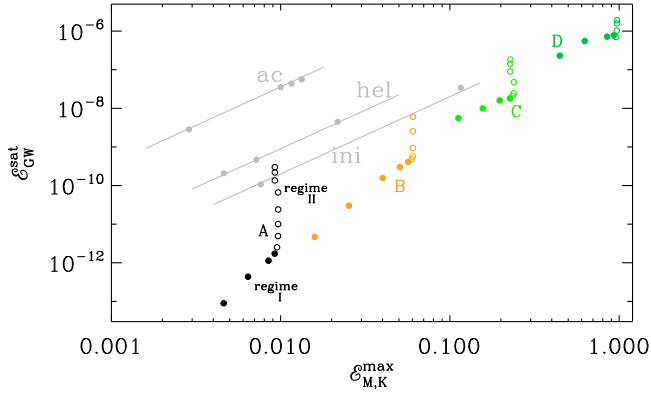**Figure 1.** $\mathcal{E}_{\mathrm{GW}}^{\mathrm{sat}}$ vs. $\mathcal{E}_{\mathrm{M}}^{\mathrm{max}}$ for runs with $\mu_{50} = 10^4$, grouped into four series with $\lambda^{1/2} = 5 \times 10^4$ (series A), 2×10^4 (series B), 10^4 (series C), and 5×10^3 (series D). In each series we vary η. Closed (open) circles refer to cases where $v_\mu/v_\lambda < 1$ (> 1), corresponding to regime I (II). For orientation, the data of Roper Pol et al. (2020b) are shown in gray; "ac" acoustic, "hel" helically forced MHD, and "ini" turbulent initial MHD state (no forcing).

where we estimate $k_{\mathrm{peak}} = k_\mu \min(1, v_\mu/v_\lambda)$. This means that $k_{\mathrm{peak}} = k_\mu$ when $v_\mu > v_\lambda$ (regime II) and $k_{\mathrm{peak}} = k_\lambda/4$ when $v_\mu < v_\lambda$ (regime I); see also Equation (13).

In view of any type of driven or decaying MHD turbulence, the dependence of $\mathcal{E}_{\mathrm{GW}}^{\mathrm{sat}}$ on η does not seem very intuitive as we find it to *increase* with increasing η, although one would have expected that a *smaller* η would cause a more vigorous time dependence. However, the increase of $\mathcal{E}_{\mathrm{GW}}^{\mathrm{sat}}$ with η is plausible due to the fact that the maximum growth rate of $\mathbf{B}$ is proportional to η, a specific of the CME.

In all of our simulations of series A–D, the parameter q is even lower than in the least efficient simulations of Roper Pol et al. (2020b). This is rather surprising and might indicate that the turbulence from the CME has a much less vigorous time dependence than the cases considered there. For understanding the reason behind this, it is necessary to study the present results in more detail by inspecting the magnetic and GW energy spectra. We begin by analyzing their mutual relation at late times when the magnetic energy has already reached a maximum and the GW energy has achieved a steady state.

3.2. Late-time GW Spectra from the CME

We consider the case of $\eta = 10^{-6}$, $\lambda = 4 \times 10^8$, and $\mu_{50} = 10^4$, which corresponds to Run B1. This means that $v_\mu = 0.01$ and $v_\lambda = 0.5$, so $v_\lambda/v_\mu = 50$, and we are clearly in regime I.

The CME leads to exponential magnetic field generation, followed by subsequent turbulent decay. At the time of the magnetic maximum, an approximate k^{-2} magnetic energy spectrum with a short inertial range develops (Brandenburg et al. 2017b). We then expect a k^{-4} spectrum for the GW energy and a k^{-6} spectrum for $\mathbf{h}$; see Roper Pol et al. (2020b). There is a trend for this to happen also in the present case, although $\mathcal{E}_{\mathrm{GW}}(k)$ does not have clear power-law subranges; see Figure 2. This is because the turbulence is not steady and both energy spectra look very different even just shortly before the magnetic field saturates, as will be shown below.

For runs in regime II, however, we find an approximate $k^{-0.5}$ profile for $E_{\mathrm{GW}}(k)$; see Figure 3. This is closer to the case of stationary turbulence; see Table 2 for a comparison of some characteristic properties. $E_{\mathrm{M}}(k)$ shows an approximate k^5 subinertial range. This is steeper than the k^4 spectrum expected
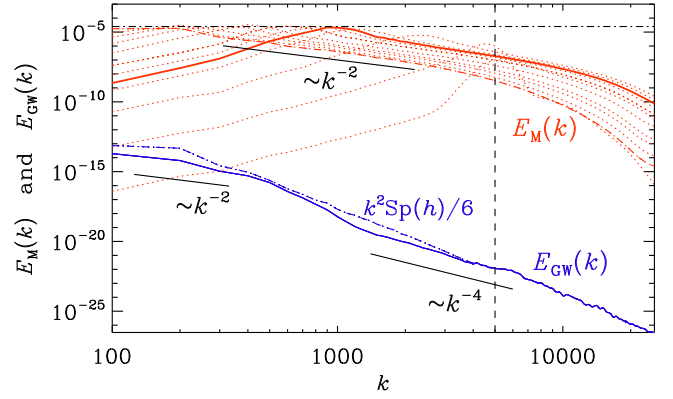

Figure 2. Magnetic and GW energy spectra for Run B1 with $\mu_{50} = 10^4$, $\lambda = 4 \times 10^8$, and $\eta = 10^{-6}$, which is in regime I with ($v_\mu = 0.01$) < ($v_\lambda = 0.5$). $E_{\mathrm{M}}(k)$ (red lines) is shown at the time of magnetic maximum (solid line, $t = 1.92$), the time when the k^{-2} spectrum is most clear ($t = 3$, dashed line), and at selected other times (dotted lines, $t = 1.71$, 1.77, 1.83, 1.89, 1.94, 2.00, 2.15, 2.32, 2.52, 2.74, and 3.00, while $E_{\mathrm{GW}}(k)$ (solid blue line) is from the simulation's end time ($t = 14$), when it can be approximated by $k^2\mathrm{Sp}(\mathbf{h})/6$ (dashed–dotted blue line). The black horizontal dashed–dotted line marks the saturation limit of Equation (10), μ_{50}/λ, and the vertical dashed line marks the position of k_μ.
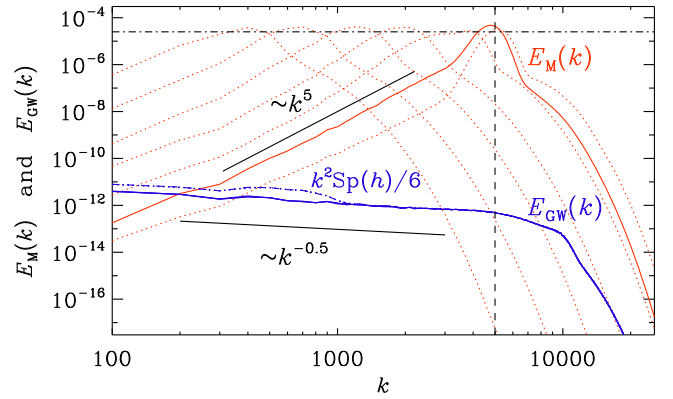

Figure 3. Similar to Figure 2, but for Run B10 with $\eta = 10^{-3}$, which is in regime II with ($v_\mu = 10$) > ($v_\lambda = 0.5$). $E_{\mathrm{M}}(k)$ (solid red line) is at the time when the magnetic energy has attained its maximum ($t = 1.001$); the red-dotted lines show $E_{\mathrm{M}}(k)$ at $t = 1.0008$, 1.003, 1.008, 1.024, and 1.075, while $E_{\mathrm{GW}}(k)$ is from the simulation's end time ($t = 1.075$), when $E_{\mathrm{GW}}(k) \approx k^2\mathrm{Sp}(\mathbf{h})/6$.

based on causality arguments (Durrer & Caprini 2003). However, as we will see more clearly later, at early times and close to $k = k_\mu$, the magnetic energy spectra show a dent, explaining therefore the apparent steeper spectrum at early times; a k^4 subinertial range can still be identified at other times. In particular, for fully helical magnetic fields, a k^4 spectrum always emerges, regardless of the initial slope; see Figure 3(a) of Brandenburg & Kahniashvili (2017).

3.3. GW Spectra during the Early Growth Phase

At early times, as discussed above, $\mathcal{E}_{\mathrm{M}}(t)$ grows exponentially at a rate of $2\gamma_0 = \eta\mu_{50}^2/2$ and $\mathcal{E}_{\mathrm{GW}}(t)$ grows at a rate of $4\gamma_0$. Across the different runs, this rate varies by three orders of magnitude. To compare the evolution of the GW and magnetic energies for the different runs, it is thus convenient to plot both quantities versus $4\gamma_0 t$. The result is shown in Figure 4 for the runs of series B. One can clearly see a slow final saturation phase of $\mathcal{E}_{\mathrm{GW}}(t)$ for all runs in regime II (Runs B7–B10), while $\mathcal{E}_{\mathrm{M}}(t)$ and $\langle\mu_5\rangle(t)$ are almost unchanged across different runs.

Table 1
Summary of Runs from Series A–G

Run	η	$\lambda^{1/2}$	μ_{50}	ηk_1	v_μ	v_λ	$\eta\mu_{50}^2$	k_1	k_λ	$\mathcal{E}_M^{max}$	$\mathcal{E}_{GW}^{sat}$	q
A1	1×10^{-6}	5×10^4	10^4	1×10^{-4}	0.01	0.2	100	100	2000	4.6×10^{-3}	8.9×10^{-14}	0.032
A2	2×10^{-6}	5×10^4	10^4	2×10^{-4}	0.02	0.2	200	100	4000	6.4×10^{-3}	4.3×10^{-13}	0.10
A3	5×10^{-6}	5×10^4	10^4	5×10^{-4}	0.05	0.2	500	100	10,000	8.5×10^{-3}	1.1×10^{-12}	0.31
A4	1×10^{-5}	5×10^4	10^4	1×10^{-3}	0.1	0.2	1000	100	...	9.2×10^{-3}	1.7×10^{-12}	0.71
A5	2×10^{-5}	5×10^4	10^4	2×10^{-3}	0.2	0.2	2000	100	...	9.5×10^{-3}	2.5×10^{-12}	1.7
A6	5×10^{-5}	5×10^4	10^4	5×10^{-3}	0.5	0.2	5000	100	...	9.6×10^{-3}	4.9×10^{-12}	2.3
A7	1×10^{-4}	5×10^4	10^4	1×10^{-2}	1	0.2	10,000	100	...	9.7×10^{-3}	1.0×10^{-11}	3.3
A8	2×10^{-4}	5×10^4	10^4	2×10^{-2}	2	0.2	20,000	100	...	9.7×10^{-3}	2.4×10^{-11}	5.1
A9	5×10^{-4}	5×10^4	10^4	5×10^{-2}	5	0.2	50,000	100	...	9.7×10^{-3}	6.6×10^{-11}	8.4
A10	1×10^{-3}	5×10^4	10^4	5×10^{-2}	10	0.2	1×10^5	50	...	9.2×10^{-3}	1.4×10^{-10}	12
A11	2×10^{-3}	5×10^4	10^4	1×10^{-1}	20	0.2	2×10^5	50	...	9.2×10^{-3}	2.2×10^{-10}	15
A12	5×10^{-3}	5×10^4	10^4	2×10^{-1}	50	0.2	5×10^5	50	...	9.2×10^{-3}	3.0×10^{-10}	18
B1	1×10^{-6}	2×10^4	10^4	1×10^{-4}	0.01	0.5	100	100	800	1.6×10^{-2}	4.7×10^{-12}	0.027
B2	2×10^{-6}	2×10^4	10^4	2×10^{-4}	0.02	0.5	200	100	1600	2.5×10^{-2}	3.0×10^{-11}	0.087
B3	5×10^{-6}	2×10^4	10^4	5×10^{-4}	0.05	0.5	500	100	4000	4.0×10^{-2}	1.6×10^{-10}	0.31
B4	1×10^{-5}	2×10^4	10^4	1×10^{-3}	0.1	0.5	1000	100	8000	5.1×10^{-2}	3.0×10^{-10}	0.68
B5	2×10^{-5}	2×10^4	10^4	2×10^{-3}	0.2	0.5	2000	100	...	5.7×10^{-2}	4.1×10^{-10}	1.4
B6	5×10^{-5}	2×10^4	10^4	5×10^{-3}	0.5	0.5	5000	100	...	6.0×10^{-2}	4.8×10^{-10}	3.7
B7	1×10^{-4}	2×10^4	10^4	1×10^{-2}	1	0.5	10,000	100	...	6.0×10^{-2}	5.6×10^{-10}	3.9
B8	2×10^{-4}	2×10^4	10^4	2×10^{-2}	2	0.5	20,000	100	...	6.0×10^{-2}	9.4×10^{-10}	5.1
B9	5×10^{-4}	2×10^4	10^4	5×10^{-2}	5	0.5	50,000	100	...	6.0×10^{-2}	2.6×10^{-9}	8.4
B10	1×10^{-3}	2×10^4	10^4	1×10^{-1}	10	0.5	1×10^5	100	...	6.0×10^{-2}	6.0×10^{-9}	12
C1	5×10^{-6}	10^4	10^4	5×10^{-4}	0.05	1	500	100	2000	1.1×10^{-1}	5.6×10^{-9}	0.33
C2	1×10^{-5}	10^4	10^4	1×10^{-3}	0.1	1	1000	100	4000	1.6×10^{-1}	9.9×10^{-9}	0.64
C3	2×10^{-5}	10^4	10^4	2×10^{-3}	0.2	1	2000	100	8000	2.0×10^{-1}	1.6×10^{-8}	1.3
C4	5×10^{-5}	10^4	10^4	5×10^{-3}	0.5	1	5000	100	...	2.3×10^{-1}	1.8×10^{-8}	3.0
C5	1×10^{-4}	10^4	10^4	1×10^{-2}	1	1	10,000	100	...	2.3×10^{-1}	2.1×10^{-8}	6.2
C6	2×10^{-4}	10^4	10^4	2×10^{-2}	2	1	20,000	100	...	2.4×10^{-1}	2.4×10^{-8}	6.6
C7	5×10^{-4}	10^4	10^4	5×10^{-2}	5	1	50,000	100	...	2.4×10^{-1}	4.8×10^{-8}	9.1
C8	1×10^{-3}	10^4	10^4	5×10^{-2}	10	1	1×10^5	50	...	2.3×10^{-1}	9.0×10^{-8}	13
C9	2×10^{-3}	10^4	10^4	1×10^{-1}	20	1	2×10^5	50	...	2.3×10^{-1}	1.4×10^{-7}	16
C10	5×10^{-3}	10^4	10^4	2×10^{-1}	50	1	5×10^5	50	...	2.3×10^{-1}	1.8×10^{-7}	18
D1	1×10^{-5}	5×10^3	10^4	2×10^{-3}	0.1	2	1000	200	2000	4.5×10^{-1}	2.3×10^{-7}	0.54
D2	2×10^{-5}	5×10^3	10^4	2×10^{-3}	0.2	2	2000	100	4000	6.3×10^{-1}	5.5×10^{-7}	1.2
D3	5×10^{-5}	5×10^3	10^4	5×10^{-3}	0.5	2	5000	100	10,000	8.5×10^{-1}	7.2×10^{-7}	2.5
D4	1×10^{-4}	5×10^3	10^4	1×10^{-2}	1	2	10,000	100	...	9.3×10^{-1}	7.7×10^{-7}	4.7
D5	2×10^{-4}	5×10^3	10^4	4×10^{-2}	2	2	20,000	200	...	9.6×10^{-1}	7.0×10^{-7}	8.7
D6	5×10^{-4}	5×10^3	10^4	1×10^{-1}	5	2	50,000	200	...	9.7×10^{-1}	1.0×10^{-6}	10
D7	1×10^{-3}	5×10^3	10^4	2×10^{-1}	10	2	1×10^5	200	...	9.7×10^{-1}	1.6×10^{-6}	12
D8	2×10^{-3}	5×10^3	10^4	4×10^{-1}	20	2	2×10^5	200	...	9.7×10^{-1}	1.9×10^{-6}	14
E1	5×10^{-6}	10^4	2×10^4	1×10^{-3}	0.1	2	2000	200	4000	4.4×10^{-1}	8.6×10^{-8}	0.67
E2	1×10^{-5}	10^4	2×10^4	2×10^{-3}	0.2	2	4000	200	8000	6.3×10^{-1}	1.5×10^{-7}	1.2
E3	2×10^{-5}	10^4	2×10^4	4×10^{-3}	0.4	2	8000	200	16,000	8.1×10^{-1}	1.9×10^{-7}	2.2
E4	5×10^{-5}	10^4	2×10^4	1×10^{-2}	1	2	20,000	200	...	9.3×10^{-1}	2.0×10^{-7}	4.9
E5	1×10^{-4}	10^4	2×10^4	2×10^{-2}	2	2	40,000	200	...	9.6×10^{-1}	2.1×10^{-7}	9.6
E6	2×10^{-4}	10^4	2×10^4	4×10^{-2}	4	2	80,000	200	...	9.7×10^{-1}	2.6×10^{-7}	10
E7	5×10^{-4}	10^4	2×10^4	1×10^{-1}	10	2	2×10^5	200	...	9.7×10^{-1}	4.6×10^{-7}	13
E8	1×10^{-3}	10^4	2×10^4	2×10^{-1}	20	2	4×10^5	200	...	9.7×10^{-1}	6.2×10^{-7}	16
F1	5×10^{-6}	10^3	2×10^3	2×10^{-4}	0.01	2	20	50	40	9.4×10^{-2}	7.2×10^{-11}	0.00091
F2	1×10^{-5}	10^3	2×10^3	5×10^{-4}	0.02	2	40	50	80	1.4×10^{-1}	6.7×10^{-9}	0.012
F3	2×10^{-5}	10^3	2×10^3	1×10^{-3}	0.04	2	80	50	160	2.5×10^{-1}	1.7×10^{-7}	0.067
F4	5×10^{-5}	10^3	2×10^3	1×10^{-3}	0.1	2	200	25	400	4.5×10^{-1}	3.3×10^{-6}	0.41
F5	1×10^{-4}	10^3	2×10^3	2×10^{-3}	0.2	2	400	25	800	6.3×10^{-1}	8.2×10^{-6}	0.91
F6	2×10^{-4}	10^3	2×10^3	5×10^{-3}	0.4	2	800	25	1600	8.1×10^{-1}	1.3×10^{-5}	1.8
F7	5×10^{-4}	10^3	2×10^3	1×10^{-2}	1	2	2000	25	...	9.3×10^{-1}	1.6×10^{-5}	4.3
F8	1×10^{-3}	10^3	2×10^3	2×10^{-2}	2	2	4000	25	...	9.6×10^{-1}	1.8×10^{-5}	8.9
G1	1×10^{-5}	5×10^2	10^3	2×10^{-4}	0.01	2	10	25	20	9.8×10^{-2}	1.1×10^{-10}	0.00054
G2	2×10^{-5}	5×10^2	10^3	5×10^{-4}	0.02	2	20	25	40	1.5×10^{-1}	7.5×10^{-9}	0.0060
G3	5×10^{-5}	5×10^2	10^3	1×10^{-3}	0.05	2	50	25	100	2.9×10^{-1}	6.0×10^{-7}	0.066
G4	1×10^{-4}	5×10^2	10^3	2×10^{-3}	0.1	2	100	25	200	4.5×10^{-1}	4.8×10^{-6}	0.24
G5	2×10^{-4}	5×10^2	10^3	5×10^{-3}	0.2	2	200	25	400	6.3×10^{-1}	1.6×10^{-5}	0.63

Table 1
(Continued)

Run	η	$\lambda^{1/2}$	μ_{50}	ηk_1	v_μ	v_λ	$\eta\mu_{50}^2$	k_1	k_λ	$\mathcal{E}_M^{max}$	$\mathcal{E}_{GW}^{sat}$	q
G6	5×10^{-4}	5×10^2	10^3	1×10^{-2}	0.5	2	500	25	1000	8.6×10^{-1}	3.9×10^{-5}	1.8
G7	1×10^{-3}	5×10^2	10^3	1×10^{-2}	1	2	1000	10	...	9.3×10^{-1}	5.4×10^{-5}	4.0
G8	2×10^{-3}	5×10^2	10^3	2×10^{-2}	2	2	2000	10	...	9.6×10^{-1}	6.2×10^{-5}	8.2

Note. The ellipses mean that k_λ exceeds μ.

Table 2
GW Spectra in Regimes I, II, and in Stationary Turbulence

Spectral Property	Run B1 Regime I	Run B10 Regime II	Station. Turb.[a]
$Sp(\dot{\mathbf{h}})/Sp(\mathbf{h})$	$0.89 \, (2\gamma_0)^2$	$0.96 \, (2\gamma_0)^2$	$0.30 \, k_f^2$
$Sp(\mathbf{T})/Sp(\dot{\mathbf{h}})$	$1.1 \, (2\gamma_0\mu_{50})^2$	$0.98 \, (2\gamma_0)^2$	$0.10 \, k_f^2$
$Sp(\mathbf{h})$, kinematic	k^{-2}	k^2	...
$Sp(\mathbf{h})$, saturated	k^{-2}	$k^{-0.5}$	k^0

Note.
[a] Run K0 of Kahniashvili et al. (2021), $k_f = 600$; the ellipsis means no growth.
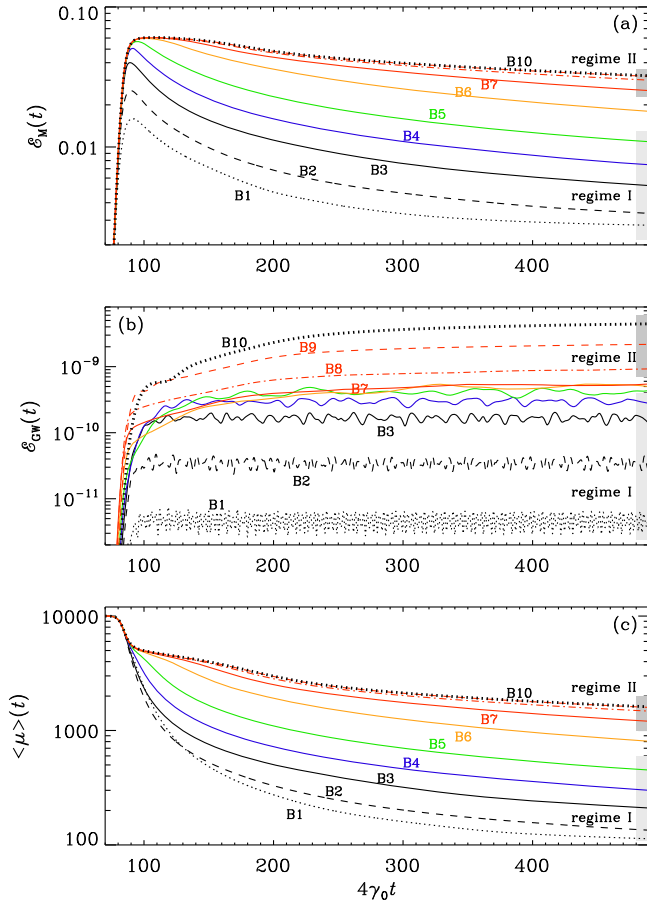
Figure 4. Evolution of $\mathcal{E}_M$, $\mathcal{E}_{GW}$, and $\langle\mu_5\rangle$ for Runs B1–B10. The light and dark gray bars on the right of each panel indicate regimes I and II, respectively. Note the occurrence of a slow final saturation phase of $\mathcal{E}_{GW}$ for all runs in regime II (Runs B7–B10). Run 8 (red dashed–dotted line), Run 9 (red-dashed line), and Run 10 (upper black-dotted line) overlap in $\mathcal{E}_M$ and $\langle\mu_5\rangle$, but are well separated in $\mathcal{E}_{GW}$.
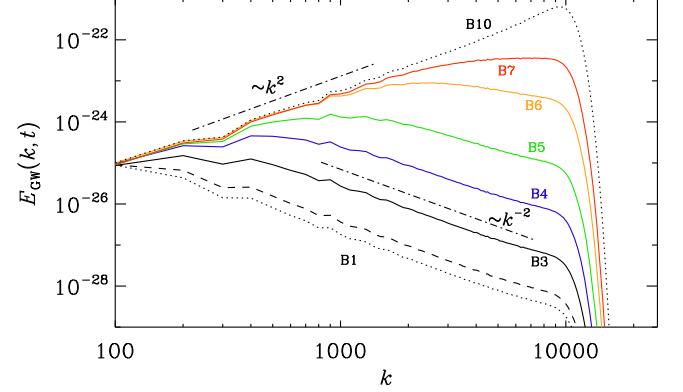
Figure 5. Comparison of the GW energy spectra during the kinematic growth stage for runs in regime I (Runs B1–B5) and regime II (Runs B7–B10). Note the change of slope at a certain wavenumber that increases as we go from regime I to regime II.

During the exponential growth phase, μ_5 is close to its initial value, $\mu_{50} = 10^4$. It drops fastest in regime I, where η is small (Runs B1–B5). However, in contrast to Figure 1, where we saw a marked qualitative change as we move from regime I to regime II, no such change is seen in Figure 4 between regime I (Runs B1–B5) and regime II (Runs B7–B10).

In the case of stationary GW spectra (see, e.g., Kahniashvili et al. 2021), and also in the previous section, we always have $Sp(\dot{\mathbf{h}}) \approx k^2 Sp(\mathbf{h}) \approx k^{-2}Sp(\mathbf{T})$, but this is not so in the early exponential growth phase. Nevertheless, in both regimes, we find $Sp(\mathbf{T}) \propto k^2$. This is a consequence of the almost monochromatic magnetic field generation in a narrow range around $k = k_\mu$, which implies that the spectral slope of $E_M(k)$ for $k < k_\mu$ is always steeper than that of white noise ($\propto k^2$), so we call it "blue noise." However, the square of a field with a blue noise spectrum always has a white noise spectrum (Brandenburg & Boldyrev 2020). This explains why $Sp(\mathbf{T}) \propto k^2$.

To see how the transition from a k^{-2} profile for small k toward a k^2 profile for large k occurs in $E_{GW}(k)$, we plot it in Figure 5 during the kinematic growth phase. The times have been arranged such that all spectra coincide at $k = k_1 \equiv 100$. We clearly see the emergence of a breakpoint from a k^2 spectrum at low k toward a k^{-2} spectrum at larger k. The breakpoint shifts toward larger wavenumbers as we go from regime I to regime II, although it can no longer be identified for Runs B7–B10.

Furthermore, in both regimes I and II, we find $Sp(\dot{\mathbf{h}}) \propto Sp(\mathbf{h})$ during the early growth phase, but their slopes are different in the two regimes. In Figures 6 and 7, we compare the spectra for Run B1 (regime I) and Run B10 (regime II), including magnetic and GW energy spectra along with the spectra of stress and strain. We clearly see that at early times, $Sp(\mathbf{h})$ and $Sp(\dot{\mathbf{h}}) = 6\mathcal{E}_{GW}(k)$
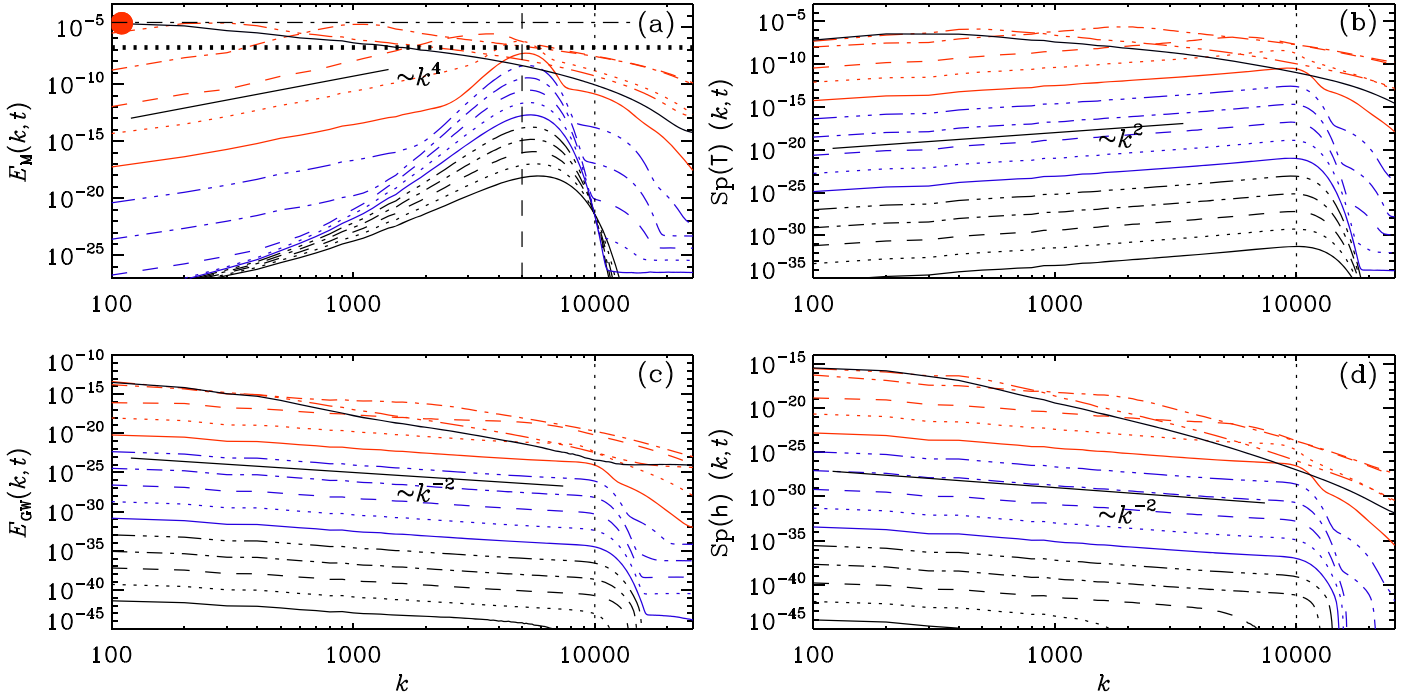
Figure 6. Time-evolving magnetic and GW energy spectra along with the spectra of stress **T** and strain **h** for Run B1 (regime I) at $t - 1 = 0.2, 0.25, 0.3, 0.35, 0.4$ denoted by black lines, 0.45, 0.5, 0.55, 0.6, 0.65 denoted by blue lines, 0.7, 0.75, 0.8, 0.9, 1.4 denoted by red lines, and the time of maximum $\mathcal{E}_M$ at 1.9, again denoted by black lines. In panel (a), the horizontal dotted line marks the level of $C_5 \mu_{50} \eta^2$, and the horizontal dashed–dotted line the level of $C_\lambda \mu_{50}/\lambda$. Vertical dotted and dashed lines mark the positions of $2k_\mu = \mu_{50}$ and k_μ, respectively. The red-filled symbol denotes the peak of $E_M(k)$ at the time of the magnetic maximum.

all have the same slope proportional to k^{-2} and k^2 in regimes I and II, respectively. Specifically, at $k = k_\mu$, we find for the ratio $\mathrm{Sp}(\dot{\mathbf{h}})/\mathrm{Sp}(\mathbf{h}) \approx (2\gamma_0)^2$ in both regimes. It is important to emphasize that, even though $\gamma(k)$ depends on k, the stress spectrum grows at the *maximum* rate γ_0 at all k. For $k \leqslant k_\mu$, this can simply be understood as a consequence of the result of Brandenburg & Boldyrev (2020) that the square of a field with a blue noise spectrum always has a white noise spectrum.

For $k > \mu_{50}$, the magnetic energy spectrum always drops rapidly. Based again on the results of Brandenburg & Boldyrev (2020), since the spectrum here is a red one, the magnetic stress spectrum also drops rapidly with the same slope. Following Brandenburg & Boldyrev (2020), in the range of $k_\mu < k < \mu_{50}$, the spectrum is slightly shallower than k^2 and it peaks at approximately $k = \mu_{50}$.

In Table 2, we summarize the spectral properties during the early kinematic growth phase and contrast it with the saturated phase. In regime I, we also find $\mathrm{Sp}(\mathbf{T})/\mathrm{Sp}(\dot{\mathbf{h}}) \approx (2\gamma_0)^2$, but in regime II, there is an extra μ_{50}^2 factor (see Table 2), which is a consequence of the different slopes of both curves. The reason for the change in the slopes in regimes I and II is explained in the next section.

3.4. Difference in the Slopes between Regimes I and II

To understand the change in the spectral slopes between regimes I and II during the kinematic growth stage it is convenient to restrict our attention to the case of a purely monochromatic exponential growth of $\mathbf{B}$ at the wavenumber k_μ with the rate $\gamma_0 = \eta \mu_{50}^2/4$. As explained in Section 3.3, the magnetic stress then increases at all k at the rate $2\gamma_0$; see also Figures 6 and 7 for a direct confirmation of this property.

Let us now assume that $\tilde{T}(\mathbf{k}, t)$, representing the Fourier transform of one of the two polarization modes of the stress, T_+

and $T_\times$, is given by

$$\tilde{T}(\mathbf{k}, t) = \theta(t - 1)\, \tilde{T}_0(k)\, e^{2\gamma_0(t-1)}, \qquad (16)$$

where $\theta(t)$ is the Heaviside step function, and $\tilde{T}_0(k)$ is assumed to depend just on $k = |\mathbf{k}|$.

Using $\tilde{h}(k, 1) = \dot{\tilde{h}}(k, 1) = 0$ as initial conditions, we can solve Equation (5) during the early growth phase in closed form as

$$\tilde{h}(k, t) = \frac{6\tilde{T}_0(k)}{4\gamma_0^2 + k^2}\left[e^{2\gamma_0 \tau} - \cos k\tau - \frac{2\gamma_0}{k}\sin k\tau \right]_{\tau = t-1}, \qquad (17)$$

where $\tilde{h}$ stands for either $\tilde{h}_+$ or $\tilde{h}_\times$. In practice, we are always interested in the case where the exponential term dominates over the cosine and sine terms. When $k \ll 2\gamma_0$, $\mathrm{Sp}(h)$ and $\mathrm{Sp}(\dot{h})$ are proportional to $\mathrm{Sp}(T_0)$. In particular, when $\tilde{T}_0(k)$ is a white noise spectrum, we have $\mathrm{Sp}(h) \propto k^2 |\tilde{T}_0(k)|^2 \propto k^2$. However, when $k \gg 2\gamma_0$, we find $\mathrm{Sp}(h) \propto \mathrm{Sp}(\dot{h}) \propto k^2 |\tilde{T}_0(k)/k^2|^2 \propto k^{-2}$, with the breakpoint being at $k_0 = 2\gamma_0$.

To compare with the results of our simulations, let us try to numerically determine the breakpoint $k = k_{GW}$ as

$$k_{GW}^{-1} = \int k^{-1} E_{GW}(k)\, dk \bigg/ \int E_{GW}(k)\, dk. \qquad (18)$$

We have calculated it for the models of series B and D and find that our analytic prediction $k_0 = 2\gamma_0$ matches the numerical results rather well; see Figure 8. Representing $\mathrm{Sp}(\dot{h})$ according to Equation (17) by

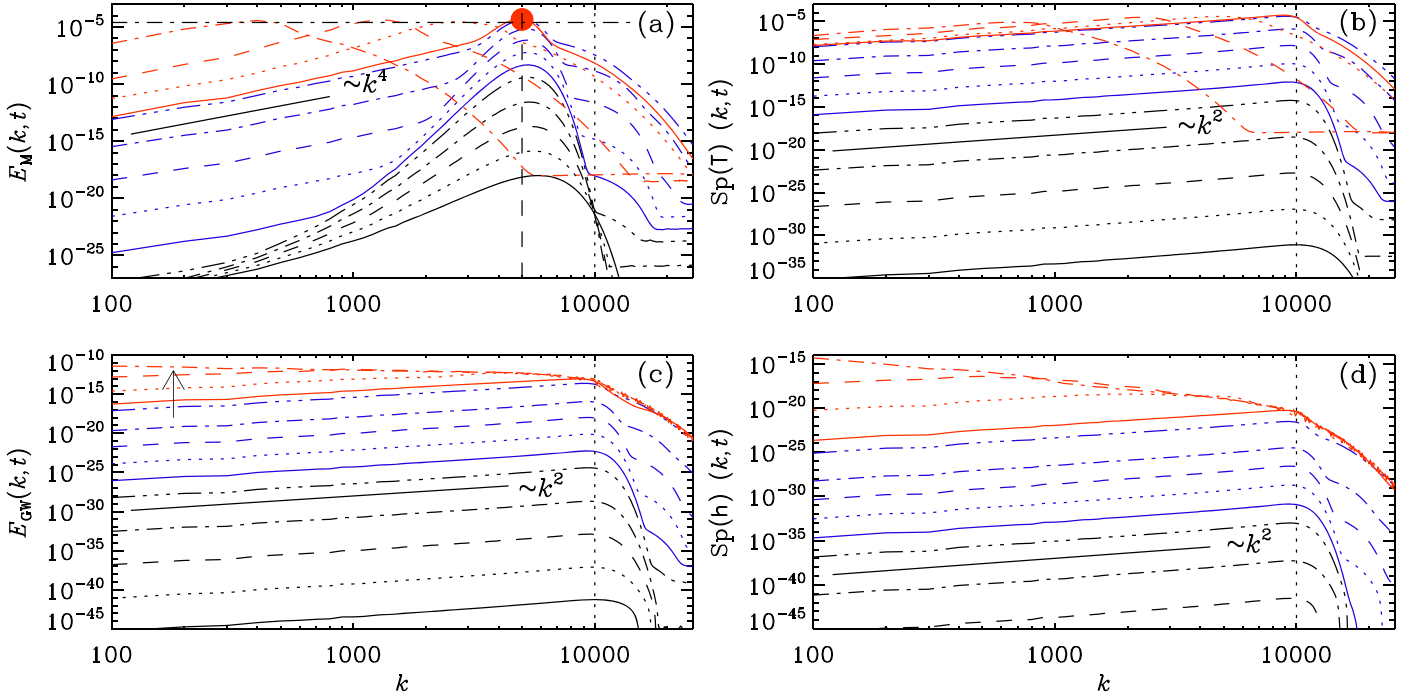$$E_{GW}^{\mathrm{model}} \propto \left[\frac{k}{k_0^2 + k^2}\, e^{-(k/\mu_{50})^4} \right]^2, \qquad (19)$$

Figure 7. Similar to Figure 6, but for Run B10 with $\eta = 10^{-3}$, which is in regime II with $(\nu_\mu = 10) > (\nu_\lambda = 0.5)$, at $t - 1 = 2, 3, 4, 5, 6 \times 10^{-4}$ denoted by black lines, 6.5, 7, 7.5, 8, 9×10^{-4} denoted by blue lines, and 0.001 (maximum $\mathcal{E}_M$), 0.002, 0.007, and 0.0075 denoted by red lines. $\mathcal{E}_M(t)$ reaches a maximum at $t - 1 = 1.1 \times 10^{-3}$ and $\mathcal{E}_{GW}(t)$ at $t - 1 = 0.02$. The upward arrow in panel (c) emphasizes the change in slope.
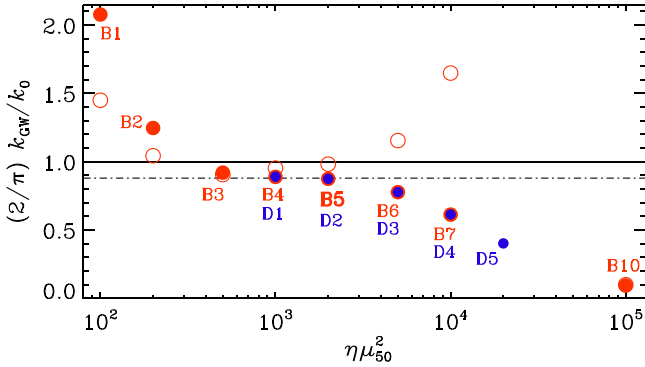
Figure 8. Dependence of k_{GW} from Equation (18), normalized by $k_0 \pi/2$, on $\eta \mu_{50}^2$ for runs of series B (red-filled symbols) and D (blue-filled symbols). Run B5 is highlighted in boldface (see Figure 9). The dashed–dotted line gives an approximate fit through the data points near their plateau, and the solid line goes through unity, the theoretically expected value. The red open symbols denote the values of k_0 obtained by fitting the spectra of Figure 5 to the model spectrum of Equation (19), similar to what is done in Figure 9.

Figure 9. Comparison of the GW energy spectrum for Run B5 and the model spectrum of Equation (19).

where the exponential factor is intended to model the cutoff near $k = \mu_{50}$, we find $k_{GW} = (\pi/2) k_0$, which is why we have compensated k_{GW} in Figure 8 by this value. The reason why there are departures for small and large values of $\eta \mu_{50}^2$ is that the wavenumber range used for the integration is limited. In addition to estimating k_0 as k_{GW} from Equation (18), we compute a fit to the model spectrum of Equation (19). We do this by minimizing the mean-squared difference between the actual spectrum and the model spectrum. Those results are also shown in Figure 8 (open symbols).

In Figure 9, we show a comparison of one of the GW energy spectra of Figure 5 with Equation (19). While it provides an
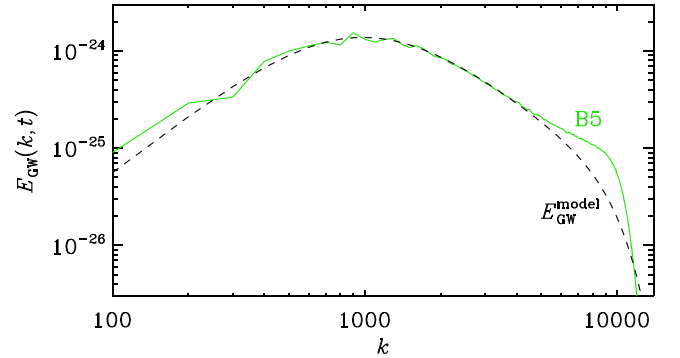
excellent description of $E_{GW}(k)$ in the bulk of the k range, the exponential factor is not sharp enough to model the simulation data near the cutoff.

3.5. Change of Slope toward Late Times

We can see in Figure 4(b) that for all runs in regime I, $\mathcal{E}_{GW}$ saturates quickly after $\mathcal{E}_M$ reaches its maximum, while for runs in regime II, $\mathcal{E}_{GW}$ continues to display a slow saturation behavior. To understand this unusual behavior, we must look again at Figure 7, showing the evolution of the spectra in Run B10, which is in regime II. We see that, at the time when $\mathcal{E}_M$ reaches its maximum, the peak of $E_M(k)$ is still at $k \approx \mu_{50}$. After that, $\mathcal{E}_M$ decays such that $\mathcal{E}_M/k_M = \text{const}$, so based on the earlier results of Roper Pol et al. (2020b), we would expect $\mathcal{E}_{GW}$ to stay constant. Looking at the evolution of $E_{GW}(k)$ for Run B10 near equilibrium in Figure 7(c), we observe a change in slope. This could be responsible for the occurrence of a slow
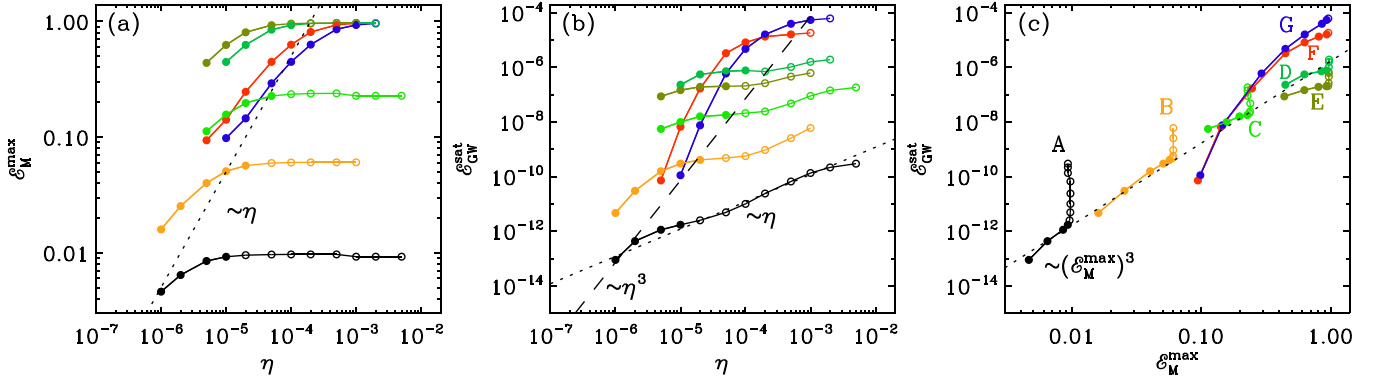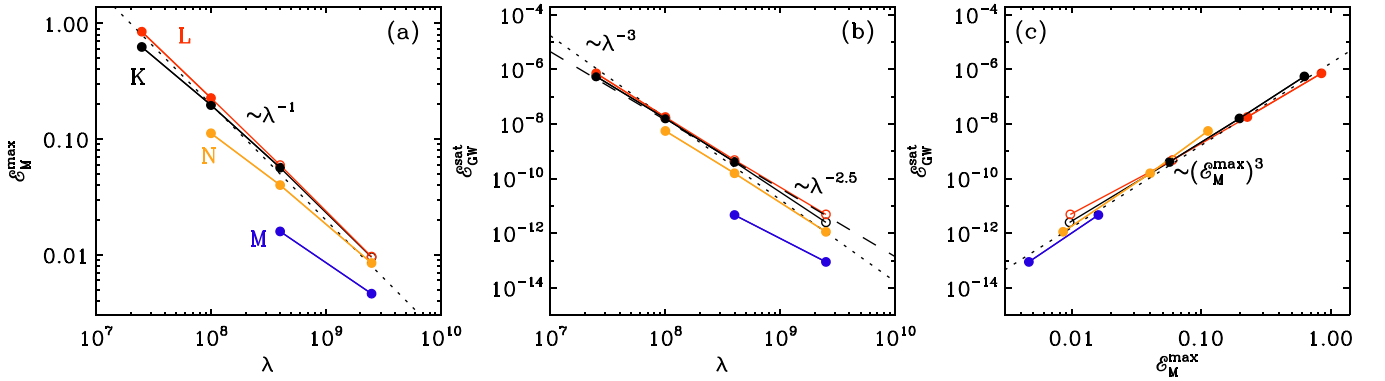
Figure 10. Dependence of $\mathcal{E}_M^{max}$ and $\mathcal{E}_{GW}^{sat}$ on η, and their mutual parametric dependence for runs of series A–D with $\mu_{50} = 10^4$ and $\lambda^{1/2} = 5 \times 10^4$, 2×10^4, 10^4, 5×10^3, respectively, series E with $\mu_{50} = 2 \times 10^4$, $\lambda^{1/2} = 10^4$, series F with $\mu_{50} = 2000$, $\lambda^{1/2} = 1000$, and series G with $\mu_{50} = 1000$, $\lambda^{1/2} = 100$. Filled (open) symbols denote the runs in regime I (II). The dotted line in panel (c) is for $q = 13 \, (\mathcal{E}_M^{max})^{1/2}$.

Figure 11. Dependence of $\mathcal{E}_M^{max}$ and $\mathcal{E}_{GW}^{sat}$ on λ, and their mutual parametric dependence for runs of series K–N. Filled (open) symbols denote runs in regime I (II). The dotted line in panel (c) is for $q = 7 \, \mathcal{E}_M^{max}$.

final saturation phase of $\mathcal{E}_{GW}$ for the runs in regime II, and especially for Run B10, seen in Figure 4.

To discuss this possibility quantitatively, let us assume a simplified spectrum of the form

$$E_{GW}(k, t_{bef}) = 3\mathcal{E}_0 \, k^2 / \mu_{50}^3 \quad \text{if } k < 2k_\mu = \mu_{50} \qquad (20)$$

for the time t_{bef} before the slope changes. For $k > 2k_\mu$ we assume a sharp falloff and therefore ignore that contribution. This k^2 spectrum is normalized such that $\int E_{GW}(k, t_{bef}) \, dk = \mathcal{E}_0$. The spectrum is then assumed to change to a new power law $\propto k^s$, with an exponent s, of the form

$$E_{GW}(k, t_{aft}) = 3\mathcal{E}_0 \, k^s / \mu_{50}^{s+1} \qquad (21)$$

for the time t_{aft} after the slope has changed. Employing the same $\mathcal{E}_0$ in Equations (20) and (21) accounts for the fact that $E_{GW}(\mu_{50}) = 3\mathcal{E}_0 / \mu_{50}$ is no longer changing in time; see Figure 7(c). For $s > -1$, the resulting GW energy is $3\mathcal{E}_0 / (s + 1)$. In Figure 3, we found that $s = -0.5$, so the resulting GW energy is then $\approx 6\mathcal{E}_0$, which is compatible with the late-time excess of $\mathcal{E}_{GW}$ in Run B10 relative to Run B6. It should be noted, however, that the change in slope occurs at a time when the magnetic field is about to reach the scale of the domain. It is therefore conceivable that $s = -0.5$ could be an artifact of the finite domain size. In particular, $s = 0$ is what has

previously been found based on numerical simulations (Roper Pol et al. 2020b) including larger domains.

3.6. Dependence on η for Given λ and μ_{50}

We have already seen that, while increasing η, we gradually move from regime I to regime II. Let us now also determine the functional dependence of both $\mathcal{E}_M^{max}$ and $\mathcal{E}_{GW}^{sat}$ on η. This is shown in Figure 10 for the runs of series A–G.

In Figure 10(c), we see the dotted line describing a cubic dependence, $\mathcal{E}_{GW}^{sat} \approx 1.7 \times 10^{-6} \, (\mathcal{E}_M^{max})^3$. A similar scaling has also been suggested by Neronov et al. (2021) based on the consideration of characteristic time and length scales. Using Equation (15), this implies a square root dependence of the efficiency parameter: $q \approx 13 \, (\mathcal{E}_M^{max})^{1/2}$.

As expected from Equation (11), smaller values of λ lead to an increase in $\mathcal{E}_M^{max}$. Values close to unity become not only more unrealistic because of big bang nucleosynthesis constraints (Grasso & Rubinstein 2001), but they also can more easily lead to numerical problems.

In all cases, we see that there is a change in slope and that $\mathcal{E}_M^{max}$ reaches a plateau when $v_\mu/v_\lambda = \eta \lambda^{1/2}$ approaches a critical value of around one half. Interestingly, $\mathcal{E}_{GW}^{sat}$ still continues to increase approximately linearly with η, so this cannot be explained by an increase in $\mathcal{E}_M^{max}$. However, we have seen in Section 3.5 that there is a change in the slope of
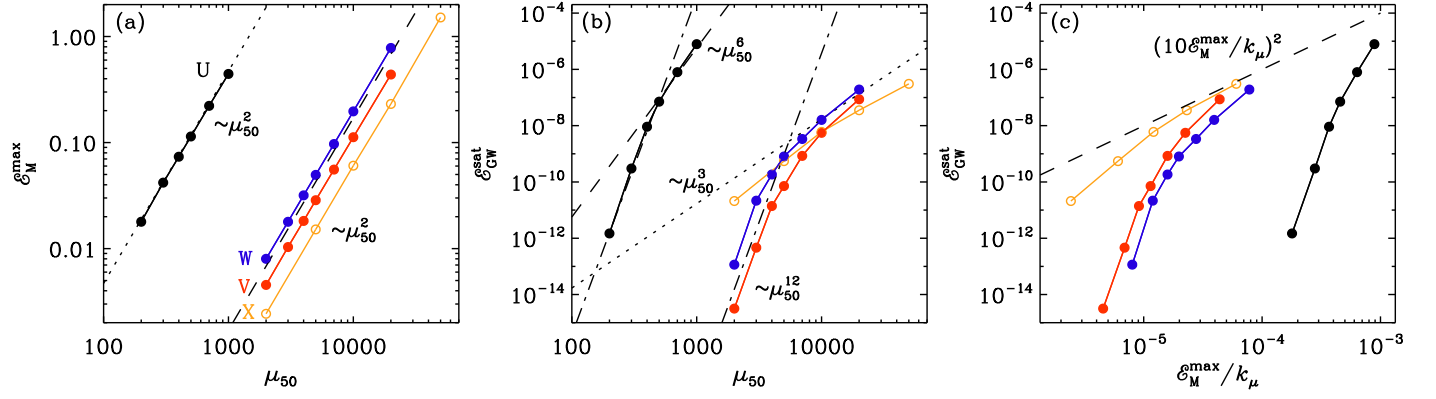
Figure 12. Dependence of $\mathcal{E}_M^{max}$ and $\mathcal{E}_{GW}^{sat}$ on μ_{50}, and their mutual parametric dependence for runs of series U–X. Filled (open) symbols denote runs in regime I (II). The dashed line in panel (c) is for $q = 10$.

Table 3
Summary of Runs from Series K–N

Run	η	$\lambda^{1/2}$	μ_{50}	ηk_1	ν_μ	ν_λ	$\eta\mu_{50}^2$	k_1	k_λ	$\mathcal{E}_M^{max}$	$\mathcal{E}_{GW}^{sat}$	q
K1	2×10^{-5}	5×10^4	10^4	2×10^{-3}	0.2	0.2	2000	100	...	9.5×10^{-3}	2.5×10^{-12}	1.7
K2	2×10^{-5}	2×10^4	10^4	2×10^{-3}	0.2	0.5	2000	100	...	5.7×10^{-2}	4.1×10^{-10}	1.4
K3	2×10^{-5}	1×10^4	10^4	2×10^{-3}	0.2	1	2000	100	8000	2.0×10^{-1}	1.6×10^{-8}	1.3
K4	2×10^{-5}	5×10^3	10^4	2×10^{-3}	0.2	2	2000	100	4000	6.3×10^{-1}	5.5×10^{-7}	1.2
L1	5×10^{-5}	5×10^4	10^4	5×10^{-3}	0.5	0.2	5000	100	...	9.6×10^{-3}	4.9×10^{-12}	2.3
L2	5×10^{-5}	2×10^4	10^4	5×10^{-3}	0.5	0.5	5000	100	...	6.0×10^{-2}	4.8×10^{-10}	3.7
L3	5×10^{-5}	1×10^4	10^4	5×10^{-3}	0.5	1	5000	100	...	2.3×10^{-1}	1.8×10^{-8}	3.0
L4	5×10^{-5}	5×10^3	10^4	5×10^{-3}	0.5	2	5000	100	10,000	8.5×10^{-1}	7.2×10^{-7}	2.5
M1	1×10^{-6}	5×10^4	10^4	1×10^{-4}	0.01	0.2	100	100	2000	4.6×10^{-3}	8.9×10^{-14}	0.032
M2	1×10^{-6}	2×10^4	10^4	1×10^{-4}	0.01	0.5	100	100	800	1.6×10^{-2}	4.7×10^{-12}	0.027
N1	5×10^{-6}	5×10^4	10^4	5×10^{-4}	0.05	0.2	500	100	10,000	8.5×10^{-3}	1.1×10^{-12}	0.31
N2	5×10^{-6}	2×10^4	10^4	5×10^{-4}	0.05	0.5	500	100	4000	4.0×10^{-2}	1.6×10^{-10}	0.31
N3	5×10^{-6}	1×10^4	10^4	5×10^{-4}	0.05	1	500	100	2000	1.1×10^{-1}	5.6×10^{-9}	0.33

$E_{GW}(k)$, which results in larger GW energy when the slope changes from k^2 to k^0 or even $k^{-0.5}$; see Equation (21).

3.7. Dependence on λ for Given η and μ_{50}

As expected, $\mathcal{E}_M^{max}$ scales inversely proportional to λ. This can be seen in the first panel of Figure 11, where we plot the runs of series K–N; see also Table 3 for a summary. In the other panels, we also show the dependence of $\mathcal{E}_{GW}^{sat}$ on λ and the mutual parametric dependence of $\mathcal{E}_{GW}^{sat}$ on $\mathcal{E}_M^{max}$. We see that the dependence of $\mathcal{E}_{GW}^{sat}$ on λ is steeper than λ^{-2}, approximately like $\propto \lambda^{-5/2}$, according to Figure 11(b). The dependence of $\mathcal{E}_{GW}^{sat}$ on $\mathcal{E}_M^{max}$ is therefore also steeper than quadratic, namely, approximately cubic; see Figure 11(c).

It is instructive to see how well the dependence of $\mathcal{E}_{GW}^{sat}$ on η, λ, and μ_{50} can be expressed just in terms of ν_λ and ν_μ. The approximately linear dependence of $\mathcal{E}_{GW}^{sat}$ on η seen in Figure 10(b) for regime II would then also suggest its linear dependence on ν_μ. Furthermore, the approximate scaling $\mathcal{E}_{GW}^{sat} \propto \lambda^{-5/2}$ seen in Figure 11(b) would suggest $\mathcal{E}_{GW}^{sat} \propto \nu_\lambda^5$. The combined dependence would then be

$$\mathcal{E}_{GW}^{sat} \propto \nu_\lambda^5 \nu_\mu, \qquad (22)$$

implying $\mathcal{E}_{GW}^{sat} \propto \mu_{50}^6$. In Section 3.9 we see that this suggestion agrees reasonably well with our data.

3.8. Dependence on μ_{50} for Given η and λ

Let us finally determine the dependence of $\mathcal{E}_M^{max}$ and $\mathcal{E}_{GW}^{sat}$ on μ_{50}, keeping η and λ unchanged. The results are shown in Figure 12. We clearly see the expected quadratic dependence of $\mathcal{E}_M^{max}$ on μ_{50}. The dependence of $\mathcal{E}_{GW}^{sat}$ on μ_{50} is much steeper and shows a break at $\mu_{50} \approx 500$ for runs of series U and 5000 for runs of series V and W. However, all those runs are in regime I; see Table 4. We have therefore added the runs of series X, which are in regime II. Nevertheless, the basic slopes are unchanged.

In Figure 12(c), we have plotted $\mathcal{E}_{GW}^{sat}$ versus $\mathcal{E}_M^{max}/k_\mu$. This allows us to estimate an upper bound for the empirical parameter q in Equation (14) if k_{peak} is replaced by k_μ. We find $q < 10$.

In view of Equation (14), using the dependence of k_{peak} on ν_μ and ν_λ, as given below Equation (15), we have $q \propto (\nu_\mu \nu_\lambda)^{1/2}$ in regime II and $q \propto (\nu_\mu^3/\nu_\lambda)^{1/2}$ in regime I. This has also been verified using our numerical data.

3.9. Combined Dependence

Equation (22) has the advantage that one can now summarize all of the numerical data in one plot. The result is shown in Figure 13. In its inset, we also show $\mathcal{E}_{GW}^{sat}$ for the set of parameters given by Brandenburg et al. (2017b) for the early universe, $\nu_\mu = 2 \times 10^{-5}$ and $\nu_\lambda = 0.05$, corresponding to

Table 4
Summary of Runs from Series U–X

Run	η	$\lambda^{1/2}$	μ_{50}	ηk_1	v_μ	v_λ	$\eta\mu_{50}^2$	k_1	k_λ	$\mathcal{E}_{\rm M}^{\rm max}$	$\mathcal{E}_{\rm GW}^{\rm sat}$	q
U1	1×10^{-4}	5×10^{2}	2×10^{2}	1×10^{-3}	0.020	0.4	4	10	40	1.8×10^{-2}	1.5×10^{-12}	0.00068
U2	1×10^{-4}	5×10^{2}	3×10^{2}	1×10^{-3}	0.030	0.6	9	10	60	4.2×10^{-2}	3.0×10^{-10}	0.0062
U3	1×10^{-4}	5×10^{2}	4×10^{2}	1×10^{-3}	0.040	0.8	16	10	80	7.4×10^{-2}	9.2×10^{-9}	0.026
U4	1×10^{-4}	5×10^{2}	5×10^{2}	1×10^{-3}	0.050	1	25	10	100	1.1×10^{-1}	7.1×10^{-8}	0.058
U5	1×10^{-4}	5×10^{2}	7×10^{2}	1×10^{-3}	0.070	1	49	10	140	2.2×10^{-1}	8.0×10^{-7}	0.14
U6	1×10^{-4}	5×10^{2}	1×10^{3}	1×10^{-3}	0.10	2	100	10	200	4.4×10^{-1}	7.9×10^{-6}	0.32
V1	5×10^{-6}	10^{4}	2×10^{3}	5×10^{-4}	0.010	0.2	20	100	400	4.5×10^{-3}	3.2×10^{-15}	0.0012
V2	5×10^{-6}	10^{4}	3×10^{3}	5×10^{-4}	0.015	0.3	45	100	600	1.0×10^{-2}	4.6×10^{-13}	0.010
V3	5×10^{-6}	10^{4}	4×10^{3}	5×10^{-4}	0.020	0.4	80	100	800	1.8×10^{-2}	1.4×10^{-11}	0.041
V4	5×10^{-6}	10^{4}	5×10^{3}	5×10^{-4}	0.025	0.5	125	100	1000	2.9×10^{-2}	7.1×10^{-11}	0.074
V5	5×10^{-6}	10^{4}	7×10^{3}	5×10^{-4}	0.035	0.7	245	100	1400	5.6×10^{-2}	8.4×10^{-10}	0.18
V6	5×10^{-6}	10^{4}	1×10^{4}	5×10^{-4}	0.050	1	500	100	2000	1.1×10^{-1}	5.6×10^{-9}	0.33
V7	5×10^{-6}	10^{4}	2×10^{4}	1×10^{-3}	0.10	2	2000	200	4000	4.4×10^{-1}	8.6×10^{-8}	0.67
W1	2×10^{-5}	10^{4}	2×10^{3}	2×10^{-3}	0.040	0.2	80	100	1600	8.0×10^{-3}	1.2×10^{-13}	0.017
W2	2×10^{-5}	10^{4}	3×10^{3}	2×10^{-3}	0.060	0.3	180	100	2400	1.8×10^{-2}	2.2×10^{-11}	0.16
W3	2×10^{-5}	10^{4}	4×10^{3}	2×10^{-3}	0.080	0.4	320	100	3200	3.2×10^{-2}	1.8×10^{-10}	0.34
W4	2×10^{-5}	10^{4}	5×10^{3}	2×10^{-3}	0.10	0.5	500	100	4000	5.0×10^{-2}	8.0×10^{-10}	0.57
W5	2×10^{-5}	10^{4}	7×10^{3}	2×10^{-3}	0.14	0.7	980	100	5600	9.7×10^{-2}	3.4×10^{-9}	0.84
W6	2×10^{-5}	10^{4}	1×10^{4}	2×10^{-3}	0.20	1	2000	100	8000	2.0×10^{-1}	1.6×10^{-8}	1.3
W7	2×10^{-5}	10^{4}	2×10^{4}	2×10^{-3}	0.40	2	8000	100	16,000	7.8×10^{-1}	1.9×10^{-7}	2.2
X1	1×10^{-3}	2×10^{4}	2×10^{3}	1×10^{-1}	2.0	0.1	4000	100	...	2.4×10^{-3}	2.1×10^{-11}	3.8
X2	1×10^{-3}	2×10^{4}	5×10^{3}	1×10^{-1}	5.0	0.2	25,000	100	...	1.5×10^{-2}	5.5×10^{-10}	7.7
X3	1×10^{-3}	2×10^{4}	1×10^{4}	1×10^{-1}	10	0.5	1×10^{5}	100	...	6.0×10^{-2}	6.0×10^{-9}	12
X4	1×10^{-3}	2×10^{4}	2×10^{4}	1×10^{-1}	20	1	4×10^{5}	100	...	2.3×10^{-1}	3.5×10^{-8}	16
X5	1×10^{-3}	2×10^{4}	5×10^{4}	5×10^{-1}	50	2	2×10^{6}	500	...	1.5×10^{0}	3.1×10^{-7}	18

$v_\lambda^5 v_\mu = 6 \times 10^{-12}$. It should be noted, however, that those values are rather uncertain because both are proportional to μ_{50}, for which only uncertain upper bounds can be proposed.

Looking at Figure 13, we see that a few runs fall outside the linear trend. This applies especially to the runs of series F and G (red-dotted and blue-dotted lines, respectively). Also the runs of series U and X (black-dashed and orange-dashed lines, respectively) show major departures. However, it is not immediately obvious what is special about them.

Looking at Figure 13, we see that data points from one series are identical with data points from another. This is because those data points are from the same runs, but have alternative names. Examples of such equivalences include Runs K1–K4 (=A5, B5, C3, D2), Runs L1–L4 (=A6, B6, C4, D3), Runs M1, M2 (=A1, B1), Runs N1–N3 (=A3, B3, C1), as well as Runs U6, V6, W6, X3 (=G4, C1, C3, B10).

3.10. Numerical Limitations

Because of certain numerical constraints, the parameters of our simulations have to stay within specific empirical limits. The purpose of this section is to discuss the nature of those constraints and to see how they depend on the choice of the parameters. Let us begin with η, which we were able to vary by more than four orders of magnitude. For smaller values of η, we go deeper into regime I, provided $\eta\lambda^{1/2} < 1$. The main limitation here is the large separation of dynamical and diffusive time scales. These time scales are proportional to μ_{50}^{-1} and $(\eta\mu_{50}^2)^{-1}$, respectively. This separation of time scales results in long run times that make the simulations more computationally costly. In addition, there is a large separation in spatial scales between μ_{50}^{-1} and η, which corresponds to large magnetic Reynolds numbers, requiring a large number of mesh
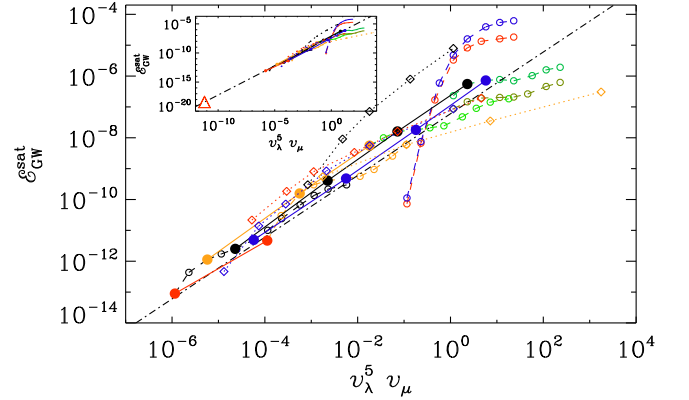

Figure 13. Dependence of $\mathcal{E}_{\rm GW}^{\rm sat}$ on $v_\lambda^5 v_\mu$ for all runs of series A–G with the same colors as in Figure 10 (dashed lines with open circles), series K–N with the same colors as in Figure 11 (solid lines with filled symbols), and series U–X with the same colors as in Figure 12 (dotted lines with diamonds). The dashed–dotted line has slope unity. The inset shows the same plot, extended down to $v_\lambda^5 v_\mu = 6 \times 10^{-12}$, corresponding to the CME estimate for the early universe, and denoted by a big red triangle in the lower left corner of the inset.

points. And as we have now seen, for decreasing η, the magnetic and GW energies become very small. For larger η, on the other hand, we go deeper into regime II, provided $\eta\lambda^{1/2} > 1$. The main limitation here is the shortness of the numerical time step, which depends on the mesh spacing δ as $\sim \delta^2/\eta$.

Next, let us discuss the value of μ_{50}, which we have been able to vary by a little over two orders of magnitude. Clearly, for the dynamo instability to exist, the mesh spacing cannot be too coarse, and μ_{50} must not exceed the largest resolved wavenumber in the domain $\pi/\delta = k_1 N/2$. Therefore, for a

given number of mesh points N, k_1 cannot be too small. It cannot be too large either because then we would no longer be able to capture the largest length scales in the system. In particular, if k_1 is too large, it could lead to artifacts resulting from the finiteness of the domain, as already discussed in Section 3.5. As we see from Table 1, we have varied k_1 by a factor of 20. It should be noted that it is not a physical parameter, since the intention is to simulate an infinitely extended domain. Therefore, the final results should be independent of k_1. An example can be seen by inspecting Figure 1 for the runs of series A, where the three uppermost open black symbols show a small shift to the left. This is because here k_1 has been decreased from 100 to 50. The problem can be even more pronounced in regime I. In Figure 2, for example, k_1 is not small enough to capture the maximum GW energy properly.

Finally, the parameter λ determines the limiting CME speed v_λ. We have varied $\lambda^{1/2}$ by over two orders of magnitude. For the smallest values in Table 1, we also needed to decrease the value of μ_{50} to prevent the magnetic energy from exceeding the critical density, which corresponds to a value of unity. This could lead to the production of shocks which, in turn, requires more mesh points, larger viscosity, or both. Furthermore, neglecting special relativistic effects could no longer be justified.

4. Conclusions

The present work has revealed a scaling relation for the GW energy from the CME: $\mathcal{E}_{\rm GW}^{\rm sat} \propto v_\lambda^5 v_\mu$. Based on earlier dimensional arguments and numerical findings for the resulting magnetic field energy (Brandenburg et al. 2017b), it was already anticipated that, within the framework of the standard description of the CME, including its dependence on temperature and the effective number of degrees of freedom, the resulting GWs would be too weak to be detectable. This is indeed confirmed by our present work. Furthermore, we have also shown that the conversion from magnetic to GW energy is generally less efficient than for forced and decaying turbulence; see Figure 1. Here, we have been able to estimate the efficiency parameter q in Equation (14) as being roughly $\propto (v_\mu v_\lambda)^{1/2}$ in regime II, but $\propto (v_\mu^3/v_\lambda)^{1/2}$ in regime I. It should also be emphasized that, even though q can reach values of the order of 10 (see Tables 1, 3, and 4), which is similar to the value for acoustic turbulence, the final GW energy production is still poor owing to the small length scales associated with the CME.

Magnetic field generation by the CME can occur in the two different regimes, I and II, depending on the relation of magnetic field generation and limiting CME speeds, v_μ and v_λ, respectively. In the present work, we have regarded the CME as a generic mechanism that allows us to study how GW energy production can be related to the strengths of generation and depletion. Whether or not other magnetogenesis mechanisms can really be described in similar ways remains to be seen. It is interesting to note, however, that our finding regarding the proportionality of the GW energy to the fifth power of v_λ is reminiscent of the earlier results of Gogoberidze et al. (2007) who found the GW energy to be proportional to the fifth power of the turbulent velocity; see their Equation (40). It should be noted, however, that the additional dependence on v_μ cannot be neglected and results in the increase of $\mathcal{E}_{\rm GW}$ with increasing values of η; see Figure 10(b).

Our work has also revealed new unexpected GW energy spectra. In regime I, the spectra were not of clean power-law form, and the spectral energy was falling off with wavenumber faster than in any earlier simulations. This means that the GW energy $\mathcal{E}_{\rm GW} = \int E_{\rm GW}(k)\, dk$ depends significantly on its lower integration bound k_1, so that it will be important to include even smaller wavenumbers in future simulations. This could restore a quadratic scaling for Runs A1–A4 and Runs B1–B5 in Figures 1 and 10(c). In regime II, on the other hand, we have seen that large GW energies can be generated. This was rather surprising and counterintuitive because this regime implies a lack of a turbulent cascade in $E_{\rm M}(k)$ with just a spectral bump traveling toward lower wavenumbers. This traveling, on the other hand, happened rather rapidly, which contributed to the large GW energies in that case. The physical reality of this regime is however questionable.

Appendix
The Compression Term in Equation (2)

At the end of Section 2.1, we noted that for $\nabla \cdot \boldsymbol{u} \neq 0$, the conservation of the total chirality requires an extra term, $-\mu_5 \nabla \cdot \boldsymbol{u}$, on the right-hand side of Equation (3). For $\Gamma_{\rm f} = 0$, this equation can then also be written as

$$\frac{\partial \mu_5}{\partial t} = -\nabla \cdot (\mu_5 \boldsymbol{u}) - \lambda \eta (\mu_5 \boldsymbol{B} - \boldsymbol{J}) \cdot \boldsymbol{B} + D_5 \nabla^2 \mu_5, \quad (A1)$$

expressing the conservation of μ_5 for $\boldsymbol{B} = \boldsymbol{0}$. To illustrate the effect of the $\mu_5 \nabla \cdot \boldsymbol{u}$ term, we consider here a simple one-dimensional example with a prescribed (kinematic) velocity field $\boldsymbol{u} = (u_0 \sin kx, 0, 0)$ and periodic boundary conditions. This is obviously an artificial way of demonstrating the consequences for the generation of $\boldsymbol{B}$. To have an effect on the conservation of μ_5, we also consider an initial profile of the form $\mu_5(x, 0) = \mu_{50} \cos kx$, so $\langle \mu_5(x, 0) \rangle = 0$. In Figure 14, we show $B_y(x)$ and $\mu_5(x)$ at $t = 10$ for $k = 1$, $\mu_{50} = 100$, $\lambda = 100$, $\eta = 10^{-3}$, and $u_0 = 10^{-2}$. We used a weak seed magnetic field with zero helicity as the initial condition.

When conservation of the total chirality is invoked by including the $\mu_5 \nabla \cdot \boldsymbol{u}$ term, there is a small enhancement of B_y
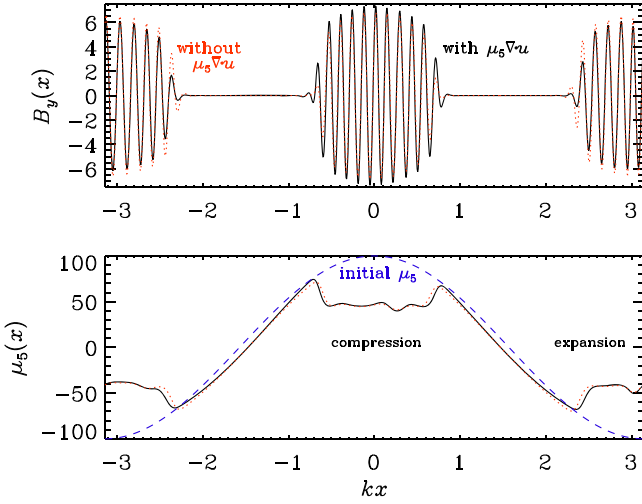
Figure 14. Comparison of the profiles of $B_y(x)$ and $\mu_5(x)$ for $k = 1$, $\mu_{50} = 100$, $\lambda = 100$, $\eta = 10^{-3}$, and $u_0 = 10^{-2}$ with (black line) and without (red-dotted line) the $\mu_5 \nabla \cdot \boldsymbol{u}$ term included. The initial profile of μ_5 is also shown (blue-dashed line).
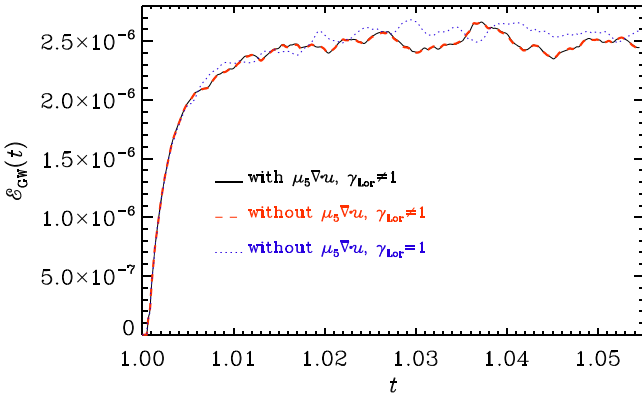

Figure 15. Comparison of $\mathcal{E}_{\mathrm{GW}}(t)$ for the cases where $\gamma_{\mathrm{Lor}} \neq 1$ and the $\mu_5 \nabla \cdot \boldsymbol{u}$ term is included (black solid line) and where it is omitted (red-dashed line) with a case where $\gamma_{\mathrm{Lor}} = 1$ and the $\mu_5 \nabla \cdot \boldsymbol{u}$ term is included (blue-dotted line).

around $kx = \pm 0.7$ and a small decrease at ± 2.3. This is caused by compression at $kx = 0$ and expansion at $kx = \pm \pi$. In this example, when the $\mu_5 \nabla \cdot \boldsymbol{u}$ term is absent, the total chirality becomes negative and reaches about 6% of its initial rms value. Finally, we show in Figure 15 the evolution of $\mathcal{E}_{\mathrm{GW}}(t)$ for Run D8, where the magnetic field is one of the largest and the effect of the $\mu_5 \nabla \cdot \boldsymbol{u}$ term is expected to be strong. We compare the case where $\gamma_{\mathrm{Lor}} \neq 1$ and the $\mu_5 \nabla \cdot \boldsymbol{u}$ term is included with a case where it is omitted, and a case where $\gamma_{\mathrm{Lor}} = 1$ and the $\mu_5 \nabla \cdot \boldsymbol{u}$ term is included. The effect of the latter is here extremely small. We also see that the inclusion of the γ_{Lor} term affects the detailed time evolution of $\mathcal{E}_{\mathrm{GW}}(t)$, but not the final overall saturation level.

ORCID iDs

Axel Brandenburg ⓘ https://orcid.org/0000-0002-7304-021X
Yutong He ⓘ https://orcid.org/0000-0001-6082-0615
Tina Kahniashvili ⓘ https://orcid.org/0000-0003-0217-9852
Matthias Rheinhardt ⓘ https://orcid.org/0000-0001-9840-5986
Jennifer Schober ⓘ https://orcid.org/0000-0001-7888-6671

References

Aharonian, F., Akhperjanian, A. G., Bazer-Bachi, A. R., et al. 2006, Natur, 440, 1018
Anand, S., Bhatt, J. R., Pandey, A. K., & Kumar, A. 2019, EPJC, 79, 119
Arnold, P., Moore, G. D., & Yaffe, L. G. 2000, JHEP, 11, 001
Boyarsky, A., Cheianov, V., Ruchayskiy, O., & Sobol, O. 2021, PhRvD, 103, 013003
Boyarsky, A., Fröhlich, J., & Ruchayskiy, O. 2012, PhRvL, 108, 031301
Boyarsky, A., Fröhlich, J., & Ruchayskiy, O. 2015, PhRvD, 92, 043004
Brandenburg, A. 2018, Pencil Code, v2018.12.16, Zenodo, doi:10.5281/zenodo.2315093
Brandenburg, A., & Boldyrev, S. 2020, ApJ, 892, 80
Brandenburg, A., Enqvist, K., & Olesen, P. 1996, PhRvD, 54, 1291
Brandenburg, A., & Kahniashvili, T. 2017, PhRvL, 118, 055102
Brandenburg, A., Kahniashvili, T., Mandal, S., et al. 2017a, PhRvD, 96, 123528
Brandenburg, A., Schober, J., Rogachevskii, I., et al. 2017b, ApJ, 845, L21
Caprini, C., Chala, M., Dorsch, G. C., et al. 2019, JCAP, 03, 024
Deryagin, D. V., Grigoriev, D. Y., Rubakov, V. A., & Sazhin, M. V. 1987, MNRAS, 229, 357
Díaz-Gil, A., García-Bellido, J., García Pérez, M., & González-Arroyo, A. 2008a, PhRvL, 100, 241301
Díaz-Gil, A., García-Bellido, J., García Pérez, M., & González-Arroyo, A. 2008b, JHEP, 2008, 043
Durrer, R., & Caprini, C. 2003, JCAP, 0311, 010
Durrer, R., & Neronov, A. 2013, A&ARv, 21, 62
Gogoberidze, G., Kahniashvili, T., & Kosowsky, A. 2007, PhRvD, 76, 083002
Grasso, D., & Rubinstein, H. R. 2001, PhR, 348, 163
Hindmarsh, M., Huber, S. J., Rummukainen, K., & Weir, D. J. 2015, PhRvD, 92, 123009
Joyce, M., & Shaposhnikov, M. 1997, PhRvL, 79, 1193
Kahniashvili, T., Brandenburg, A., Gogoberidze, G., Mandal, S., & Roper Pol, A. 2021, PhRvR, 3, 013193
Kahniashvili, T., Tevzadze, A. G., Brandenburg, A., & Neronov, A. 2013, PhRvD, 87, 083007
Kosowsky, A., Mack, A., & Kahniashvili, T. 2002, PhRvD, 66, 024030
Neronov, A., Roper Pol, A., Caprini, C., & Semikoz, D. 2021, PhRvD, 103, L041302
Neronov, A., & Vovk, I. 2010, Sci, 328, 73
Okano, S., & Fujita, T. 2021, JCAP, 03, 026
Pencil Code Collaboration, Brandenburg, A., Johansen, A., et al. 2021, JOSS, 6, 2807
Rogachevskii, I., Ruchayskiy, O., Boyarsky, A., et al. 2017, ApJ, 846, 153
Roper Pol, A., Brandenburg, A., Kahniashvili, T., Kosowsky, A., & Mandal, S. 2020a, GApFD, 114, 130
Roper Pol, A., Mandal, S., Brandenburg, A., Kahniashvili, T., & Kosowsky, A. 2020b, PhRvD, 102, 083512
Schober, J., Brandenburg, A., & Rogachevskii, I. 2020, GApFD, 114, 106
Schober, J., Rogachevskii, I., Brandenburg, A., et al. 2018, ApJ, 858, 124
Sharma, R., Subramanian, K., & Seshadri, T. R. 2020, PhRvD, 101, 103526
Taylor, A. M., Vovk, I., & Neronov, A. 2011, A&A, 529, A144
Vilenkin, A. 1980, PhRvD, 22, 3080